論文 / 著書情報
Article / Book Information

題目(和文)	「すざく」衛星で観測されたX線バーストによる中性子星の質量半径関係への制限
Title(English)	Constraints on the Mass-Radius Relation of Neutron Stars from Thermonuclear X-ray Bursts Observed with Suzaku
著者(和文)	岩井將親
Author(English)	Masachika Iwai
出典(和文)	学位:博士(理学), 学位授与機関:東京工業大学, 報告番号:甲第10053号, 授与年月日:2016年3月26日, 学位の種別:課程博士, 審査員:堂谷 忠靖,河合 誠之,松原 英雄,垣本 史雄,中村 隆司
Citation(English)	Degree:Doctor (Science), Conferring organization: Tokyo Institute of Technology, Report number:甲第10053号, Conferred date:2016/3/26, Degree Type:Course doctor, Examiner:,,,,
学位種別(和文)	博士論文
Type(English)	Doctoral Thesis

Ph.D. Thesis

Constraints on the Mass-Radius Relation of Neutron Stars from Thermonuclear X-ray Bursts Observed with Suzaku

Masachika Iwai

Department of Physics,
Graduate School of Science and Engineering,
Tokyo Institute of Technology

December 2015

Abstract

Extreme conditions that are not possible in the ground experiments are sometimes realized in the universe. A good example is a neutron star, the end product of the supernova explosion of a massive star. A neutron star is a very compact object supported by the degeneracy pressure of neutrons. Because the internal density of a neutron star may exceed that of atomic nuclei, it is best suited to probe the nature of the ultra-dense matter. For that purpose, precise measurements of the mass-radius relation of a neutron star are required. Instead of directly measuring the mass and radius, we can measure the mass-radius ratio, i.e. gravitational redshift at the neutron star surface, because it is little affected by systematics among various methods. If we can detect spectral features in the emission from the photosphere of a neutron star, their apparent energies compared to the theoretical values directly give the gravitational redshift at the neutron star surface. Spectral features may be preferentially produced during the thermonuclear X-ray bursts, especially those with photospheric-radius expansion, because the temperature structure of the bursting atmosphere and the production of heavy elements are suited to form the spectral features.

For this purpose, we systematically analyzed the Suzaku archival data looking for the thermonuclear X-ray bursts. A thermonuclear X-ray burst with photospheric-radius expansion was serendipitously detected from GRS 1747−312, a low-mass X-ray binaries located in the globular cluster Terzan 6. The sky field including the source was covered as a part of the Galactic bulge mapping observations, and the X-ray burst showed a long duration with moderate photospheric-radius expansion.

The burst spectra were reproduced by the conventional model of the absorbed blackbody most of time, but significant deviation was detected in the late cooling phase. The energy spectra showed a clear roll-off above $\sim$7 keV. We examined various models to reproduce the spectral feature including non-Planckian burst spectra, partial covering absorption, and Doppler-smeared absorption edges due to the rapid spin of a neutron star.

We found that the Doppler-smeared absorption edges are most plausible as they can naturally explain the presence of the feature only in the late cooling phase of this particular burst. According to this scenario, the burst ashes, containing Fe and Zn, are exposed on the neutron star surface during the photospheric-radius expansion phase. We estimated the surface gravitational redshift of the neutron star, based on the above identification of the elements that were responsible for the observed edges. We discuss implication of the estimated gravitational redshift and possible constraints on the mass-radius relation of neutron stars. Because the absorption edge is not completely smeared out despite of the rapid spin of the neutron star, this can be a powerful tool to measure the gravitational redshift of neutron stars.

Contents

List of Figures

List of Tables

Chapter 1

Introduction

In this chapter, we will review neutron stars making stress on thermonuclear X-ray bursts from an observational point of view. In addition to the review, we will summarize the methods and past studies to constrain the mass-radius relation of neutron stars, which are main topics of this thesis.

1.1 Neutron Stars

1.1.1 What is a neutron star?

A neutron star is a very compact object and it serves as natural laboratories for ultra-dense matter. It is the collapsed core of a massive star left behind the supernova explosion at the end of their nuclear fusion lifetimes and is supported by degeneracy pressure of neutrons. Its mass and radius are, typically, 1.4 $M_\odot$, where $M_\odot \simeq 2 \times 10^{30}$ kg is the solar mass, and the order of 10 km, respectively. Its internal density may exceed that of atomic nuclei and therefore it is best suited to probe the nature of the ultra-dense matter.

1.1.2 Surface and Internal Structure of a Neutron Star

A neutron star can be split into five main layers: a thin atmosphere, an outer crust, an inner crust, an outer core liquid, and an inner core. Figure 1.1 shows a schematic view of a neutron star with the surface and internal structure. The surface is covered by a thin atmosphere, which contains light elements (mainly H and/or He). The outer crust, starting from the surface, composed by atomic nuclei and free electrons. The next layer is the inner crust, where free neutrons add to the atomic nuclei and free electrons form a very dense solid layer. Deeper down there is the outer core liquid, where free electrons, neutrons, protons and muons co-exist in a nuclear soup. The last layer is the inner core, where, for densities exceeding that of a nucleus, there are several exotic possibilities, involving existence of pions, kaons, hyperons and even, in extreme densities, quark matter. The internal structure of a neutron star can, in principle, be probed by a distant observer, but it is still poorly understood.

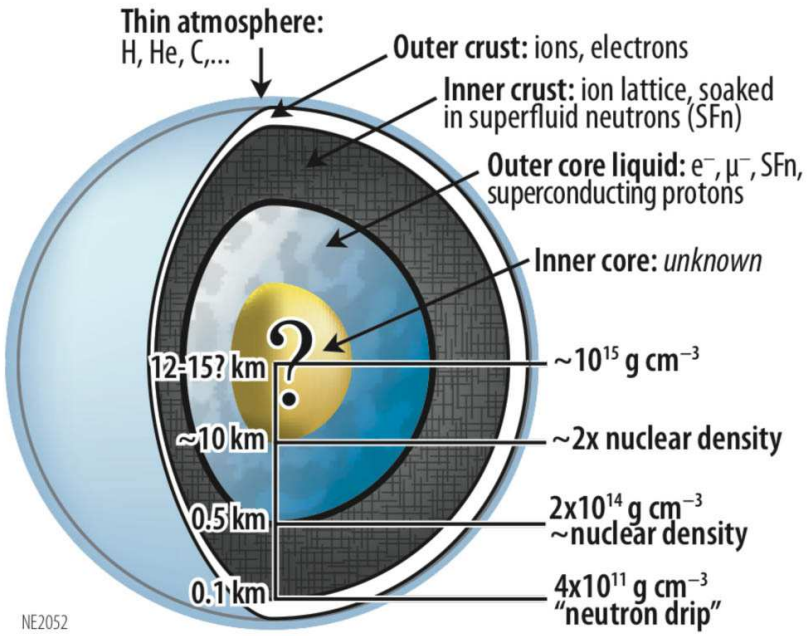

Figure 1.1: Schematic view of a neutron star with the surface and internal structure.[1]

1.1.3 Variety of Neutron Stars

Empirically, neutron stars can be divided into four classes, according to the primary power source for their emission: rotation-powered pulsars emit their energy primarily by the rotation of the neutron stars, magnetars by magnetic field energy, isolated hot neutron stars by the latent heat of the matter of the neutron stars, and accretion-powered neutron stars by the energy released by matter accreting onto the neutron star from a binary companion. Although such classification of neutron stars is convenient to understand the nature of the sources, it is not directly connected to the observable parameters such as a rotation period P and a surface magnetic field B. In reality, as shown in figure 1.2, these classes of sources occupy different region in the P-B diagram. Some neutron stars are also known to switch between these classes during their evolution, e.g., between rotation-powered neutron stars and accretion-powered neutron stars. Details of each class will be described in the following sub-sections.

1.1.3.1 Rotation-powered neutron stars

Rotation-powered neutron stars are spinning down as a result of torques from magnetic dipole radiation and particle emission. The energy from their spin down appears as broad-band pulsations from radio to gamma-ray wavelengths and as a wind of energetic particles flowing into their surrounding pulsar wind nebulae.

[1] http://heasarc.gsfc.nasa.gov/docs/nicer/nicer_about.html

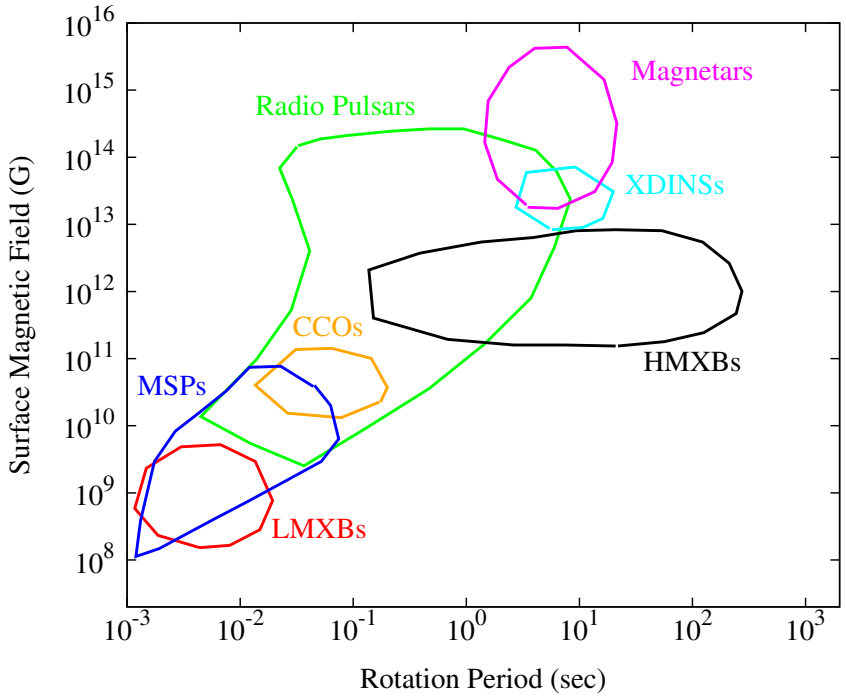

Figure 1.2: Schematic populations of various neutron stars with respect to their rotation period P and surface magnetic fields B, which is adopted from Harding (2013).

More than 2000 rotation-powered neutron stars are now known[2]and they show a young characteristic age, a typical magnetic field of $B \sim 10^{12}$ G, and periods ranging from a few ms to several seconds. Those with periods of a few ms, especially, are called as millisecond pulsars (MSPs) and their pulse profiles and energy spectrum have been used to constrain the compactness of neutron stars (section 1.4.3).

1.1.3.2 Accretion-powered neutron stars

Accretion-powered neutron stars are forming binary systems and their primary power source is the energy released by matter accreting onto a neutron star from a binary companion. They show old characteristic age and are traditionally divided into two sub-classes, according to the mass of companion stars. One sub-class is a neutron star in a low-mass X-ray binary (LMXB) system (Lewin et al. 1993). In the system, the neutron star is weakly magnetized (10^8–10^9 G) and its companion star has a small mass of $M \leq 1$ $M_\odot$. The luminosity is powered gravitationally by accreting matter from Roche-lobe overflow. Details of the LMXB system are described in section 1.2.2. The other is a neutron star in a high-mass X-ray binary (HMXB) system, which is often called as an X-ray pulsar. In the system, the neutron star is strongly magnetized (10^{12}–10^{13} G) and its companion star has a

[2]http://www.atnf.csiro.au/people/pulsar/psrcat/

large mass of $M \geq 20$ $M_{\odot}$. The luminosity is powered gravitationally by accreting matter from the stellar wind of companion stars, in addition to Roche-lobe overflow, due to the strong magnetosphere. At present, 114 HMXBs are known in the Galaxy (Liu et al. 2006). Among them, about 20 HMXBs show (harmonic) absorption features caused by the electron cyclotron resonance. Measurements of these resonance energies provide the most reliable knowledge on the magnetic field strengths of these sources.

1.1.3.3 Magnetically-powered neutron stars

Magnetically-powered neutron stars are isolated ones with ultra-strong magnetic fields (10^{14}–10^{16} G), which are often called as magnetars (see, e.g., Enoto et al. 2010). This extreme magnetic field powers their bright emission, rather than accretion or rotational power as for most of the X-ray pulsars. They sometimes emit repetitive short burst, and on rare occasions, giant flares which are so energetic as to disturb the Earth's ionosphere. At present, about 20 magnetars are found, which contains Anomalous X-Ray Pulsars and Soft Gamma-Ray Repeaters. These sources which have been considered thought for many years to be separate and unrelated objects are now considered to be both neutron stars possessing magnetic fields of unprecedented strength, i.e. sub-classes of magnetars.

1.1.3.4 Isolated hot neutron stars

Neutron stars powered by the latent heat of their matter are observed as various types of X-ray sources including X-ray dim isolated neutron stars (XDINS) and Compact Central Objects (CCOs). XDINSs are very nearby neutron stars that appear to be thermally cooling with dominant soft X-ray and faint optical/UV emission. There are presently seven confirmed XDINS, six of which show weak X-ray pulsations with periods of a few seconds. CCOs are soft X-ray sources located close to the centers of young supernova remnants. They have no apparent emission other than soft X-ray band and no binary companion. About ten CCOs are known at present and several CCOs show pulsations at hundreds of milliseconds. Although exciting results over the past few years have brought these two types of sources into the forefront of the studies on neutron stars, they are still poorly understood.

1.2 Thermonuclear X-ray Bursts

Thermonuclear X-ray bursts are key phenomena to probe the nature of ultra-dense matter, and are the main topic in this thesis. In this section, we review thermonuclear X-ray bursts from both observational and theoretical sides.

1.2.1 What is a thermonuclear X-ray burst?

Thermonuclear X-ray bursts (hereafter X-ray bursts[3]) are runaway thermonuclear reaction on the surface of neutrons stars. They are characterized by a sudden increase of X-ray luminosity, which is brighter by orders of magnitude than those before the burst, followed by a gradual decrease. Typically, rise times, which indicate an interval from the burst onset to the peak of burst flux, range within ≈10 seconds and decay times range from a few ten seconds to a few hundred seconds. Their recurrence times range from several hours to several days, depending on the mass accretion rates. In a single X-ray burst, the total energy of $10^{39} - 10^{40}$ ergs is released. Some bursts reach the luminosity of the Eddington limit, at which the radiation pressure balances the gravitational force of a neutron star.

These events are caused by unstable burning of accreted matter on the neutron star surface (Lewin, van Paradijs & Taam et al. 1993). They typically occur in LMXBs, but they do not occur in very bright LMXBs, where the luminosity exceeds a fraction of the Eddington limit. This is because the temperature on the neutron star surface in such bright LMXBs is persistently so high that the accreted matter burns stably. Similarly, no X-ray burst occurs in HMXBs, because accreted matter is intensively funneled onto the magnetic poles and the temperature there is sufficiently high. Details of the LMXBs will be explained in the following subsection.

1.2.2 Low-Mass X-ray Binaries (LMXBs)

LMXBs are close binary systems and consisting of two stars that are gravitationally bound to each other. One is a compact star, i.e. either a weakly magnetized neutron star ($B \approx 10^{8-9}$ G) or a black hole. In this thesis, we focus on the neutron star in LMXBs. The other is a companion star which is a late-type main-sequence star with a mass of $\lesssim M_\odot$. At present, a total of 187 LMXBs are known in the Galaxy (Liu et al. 2007). They are concentrated in the direction of the Galactic center and, furthermore, frequent in the globular clusters.

In these LMXBs system, a mass accretion from a companion star to a neutron star usually occurs and it often causes the above-mentioned X-ray bursts. Figure 1.3 shows a schematic view of a LMXB system. Forming an accretion disk around the neutron star, matters from a companion star is accreted onto a NS

[3]In reality, X-ray bursts are classified into two types: one is associated with the thermonuclear X-ray flashes and the other is linked to accretion instabilities. However, as the latter is not described further in this thesis, we will refer "thermonuclear X-ray bursts" as simply "X-ray bursts"

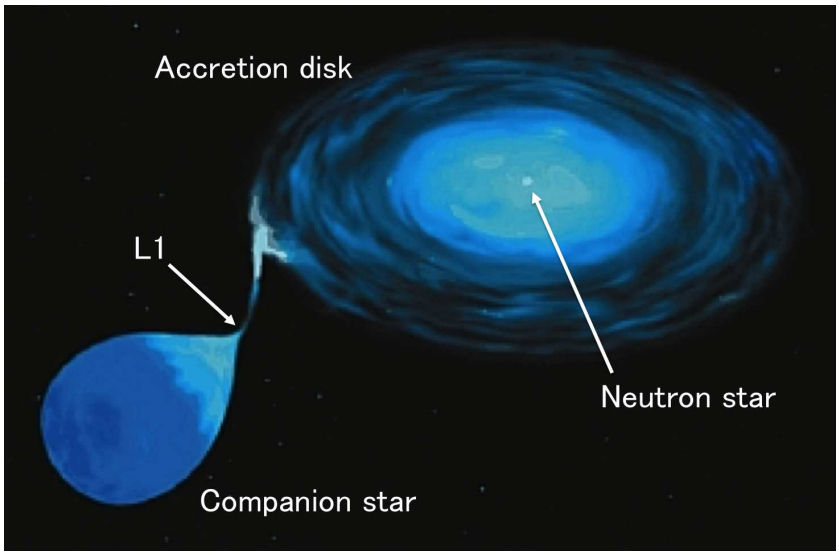

Figure 1.3: Schematic configuration of a low-mass X-ray binary system (LMXB).

by Roche-lobe overflow. This Roche-lobe overflow occurs through the inner Lagrangian point L1, which corresponds to the inner saddle point of the effective potential. As a result, a large amount of X-rays are emitted around the neutron star because of its strong gravitational field. Furthermore, they also show some characteristic profiles, e.g. dips, eclipses, outbursts, and X-ray bursts. The X-ray emission of LMXBs contains crucial information about the properties of these system and neutron stars themselves.

LMXBs are considered to be the progenitors of the majority of millisecond pulsars. The population of LMXBs overlap with those of the millisecond pulsars in the spin period versus magnetic field strength diagram (P-B diagram): LMXBs and millisecond pulsars both have very weak magnetic fields and the shortest periods, compared with those of other types of neutron stars. Furthermore, most of millisecond pulsars form binary systems as LMXBs do. These observational facts proposed a scenario that LMXB is a possible progenitor of millisecond pulsar. This scenario is often called as "recycling scenario", which is now generally accepted (see, e.g., Bhattacharyya & van den Heuvel 1991 for a review). In this scenario, firstly, a more massive star in a binary system evolves and forms a radio pulsar as the end product of a supernova explosion. The pulsar spin up under the magnetic dipole emission and switches off when it eventually crosses the death line in the P-B diagram, below which the radio pulsar phenomenon does not take place (dead). Meanwhile, the less massive companion evolves until it reaches its giant state, during which it transfers mass onto the dead pulsar. During this mass accretion, the pulsar also receives angular momentum and back across the death line (recycling). During this phase, the system is visible as a LMXB. Eventually, the pulsar starts emitting radio emission again and furthermore spin it up to millisecond pulsars.

1.2.3 Observational Properties

Many X-ray bursts have been observed by various X-ray satellites since their discovery over 40 years ago. Especially, observational studies of X-ray bursts showed a lot of progress with the Rossi X-ray Timing Explorer (RXTE), whose main results are summarized in Galloway et al. (2008). At present, a total of 105 X-ray burst sources are identified in Galaxy, according to a catalogue of X-ray burst sources by in't Zand[4]. Most of them have been found in the Galactic bulge region. Some X-ray bursts exhibit several peculiar phenomena which lead to constrains on the mass-radius relation of neutron stars: a photospheric radius expansion, super bursts, and a burst oscillation. These phenomena will be described below.

1.2.3.1 Photospheric radius expansion bursts (PRE bursts)

In some bright X-ray bursts, their luminosities reach the Eddington limit and they show photospheric radius expansion (PRE). Once the luminosity exceeds the Eddington limit, the excess energy is transformed to the kinetic energy of the atmosphere on a neutron star. As a result, the atmosphere is lifted off the surface of the neutron star for a certain period. Such bursts are particularly called as PRE bursts, which are roughly about 20% of all X-ray bursts. Most of them show moderate PREs by a factor of a few, while a small fraction of them show extreme PREs (superexpansion) by a factor of 100 or more, which corresponds to the radii of photosphere above $\sim 10^3$ km.

Figure 1.4 shows an example of time-evolutions of the spectral parameters during a PRE burst. In general, a PRE burst is divided into the following two phases. One is a PRE phase. During this phase, the luminosity remains nearly constant (the Eddington limit). The apparent radius expands just after the burst and reach the peak, and then contracts gradually and eventually return to the neutron star surface (Touch-down). The color-temperature is anti-correlated with the apparent radius. According to whether the apparent radius expands or contracts, the phase can also be divided into further two sub-phases: a radius-rising phase and a radius-contraction phase. The other is a cooling phase following the PRE phase. During this phase, the apparent radius remains constant, which corresponds to the radius of a neutron star. The color-temperature and the luminosity, which is proportional to the forth power of the color-temperature, both decays with time.

1.2.3.2 Superbursts

Superbursts are bursts of an extreme-long duration, which are associated with the unstable thermonuclear burning of a carbon-rich layer. They show timescales of a few hours, recurrence times of a few years, and energetics of 10^{41}–10^{42} ergs, unlike the normal X-ray bursts (Strohmayer & Brown 2002; Cumming 2004). These are probably due to the difference of fuel composition, i.e. carbon. Only about 24 (candidate) superbursts from 14 different X-ray burst sources have been observed so far, referring to the catalogue of X-ray burst sources by in't Zand.

[4]https://personal.sron.nl/∼jeanz/bursterlist.html

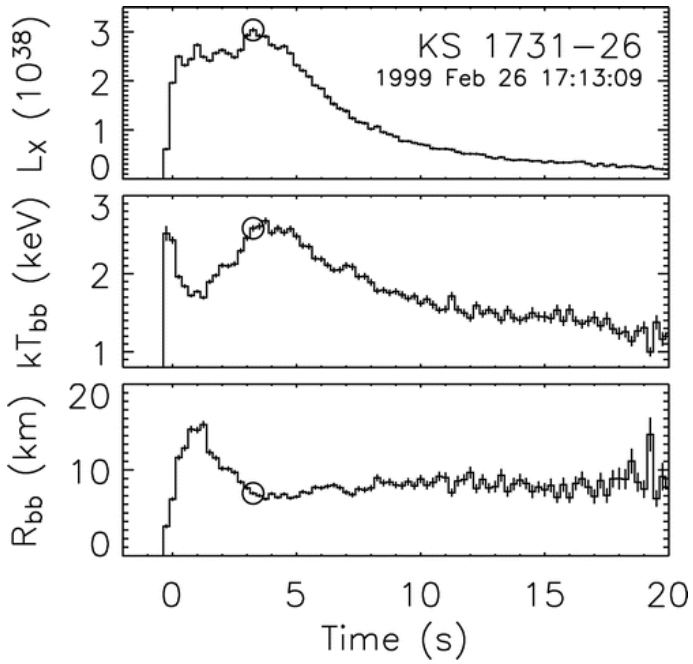

Figure 1.4: An example of time-evolutions of the spectral parameters during a burst with photospheric-radius expansion (PRE): a luminosity, a color-temperature, and an apparent radius, from top to bottom (Galloway et al. 2008).

1.2.3.3 Burst Oscillations

Some X-ray bursts exhibit periodic fluctuations in their light curves, which are called burst oscillations. They have been detected during the radius-rising phase and/or the decay phase of X-ray bursts. The oscillations during the radius-rising phase may be consistent with the spreading of a hot spot on a rotating neutron star. On the other hand, those during the decay phase exhibit a drift in frequency, increasing by a few Hz and approaching an asymptotic value as the burst progresses. The asymptotic frequency seems to be a spin frequency of a neutron star, because the oscillations have also been observed in the bursts from millisecond pulsars with well-known spin frequencies and their asymptotic frequencies are consistent with the spin frequencies of the neutron stars. The spin frequencies of X-ray bursters measured from the burst oscillations all range between 270–620 Hz (Strohmayer 2001). Furthermore, the amplitude and the shape of a phase-folded burst oscillation light curve can be useful to constrain the mass-radius relation of neutron stars. Details of the measuring method will be presented in section 1.4.3.

1.2.4 Models of the X-ray Bursts

X-ray bursts are runaway thermonuclear reaction on the neutron star surface which receives mass-accretion from the companion star, as explained in section 1.2.1. The accreted hydrogen and helium accumulates on the neutron star surface and periodically ignites to cause run-away burning. The regimes of thermonuclear

ignition is roughly classified into three cases (Fujimoto et al. 1981) according to the mass accretion rates, $\dot{M}$, that is often expressed as a fraction of those corresponding to the Eddington limit, $\dot{M}_{\rm Edd}$ (1.3×10^{-8} $M_\odot$ yr^{-1} averaged over the surface for an assumed radius of a neutron star, 10 km):

- At the regime of low accretion rates, i.e. $\dot{M} < 0.01\dot{M}_{\rm Edd}$, He-burning are triggered by thermally unstable H-ignition. In this regime, the temperature in the accreted layer is too low for stable H-burning between bursts. Hydrogen ignites unstably, triggering He burning and giving rise to X-ray burst in a H-rich environment.

- At the intermediate accretion rates, i.e. $0.01\dot{M}_{\rm Edd} < \dot{M} < 0.1\dot{M}_{\rm Edd}$, pure He-burning follows completion of H-burning. Here, the temperature in the accreted envelope is higher and H burns steadily to He between X-ray bursts. The bursts occur as a consequence of He ignition in a pure He layer.

- At the high accretion rates, i.e. $0.1\dot{M}_{\rm Edd} < \dot{M}$ He-burning is triggered by thermally unstable He-ignition. Here, accretion provides fresh H fuel at a rate higher than the steady burning. He ignites in a mixed H/He environment.

Although quantitative comparison between models and observations is not necessarily successful (see, e.g., Fujimoto et al. 1987; Bildsten 2000), X-ray bursting models successfully explain the burst properties, e.g. recurrence times, energetics, and durations (Lewin, van Paradijs, & Taam 1995 ; Bildsten 1998).

1.2.4.1 Nucleosynthesis in X-ray Bursts

Model calculations of X-ray bursts have been performed using extensive nuclear reaction network. The main nuclear reaction of He-burning is driven by the following three process: the rp-process (rapid proton-captures and β^+_ decays), the 3α-reaction, and the αp-process (a sequence of (α, p) and (p, γ) reactions). Figure 1.5 shows an example of the simplified nuclear reaction network during an X-ray burst. This figure demonstrates that the rp-process is significantly contributed to produce the heavy nuclei up to and beyond the iron group. In the figure, although all flow converge upon ^{56}Ni nucleus and only a small leak continues on to higher masses, the end products of an X-ray burst are very sensitive to input parameters and the composition of the subsequent burst products, as mentioned later. Only very recently has it been possible to couple a spherically symmetric (one-dimensional) hydrodynamic stellar calculations and detailed nuclear reaction networks. Recent efforts include Woosely et al. (2006) with networks of 1300 isotopes (up to Po) and an adoptive network, Jose et al. (2010) networks of 325 isotopes (up to Te) and 1392 nuclear processes, and so on.

Figure 1.6 shows examples of the nucleosynthesis calculations of the envelope at a mass accretion rate of $\sim 0.1\dot{M}_{\rm Edd}$ and each burst light curve (Parikh et al. 2013). These calculations were performed for the different metalicities Z, which indicates the mass faction of heavy elements (C, N, and O), of the accreted matter: accreting solar-like material ($Z = 0.02$) and accreting material of lower metalicities ($Z = 10^{-3}$). The bursts for accreted material of lower metalicity shows lower peak

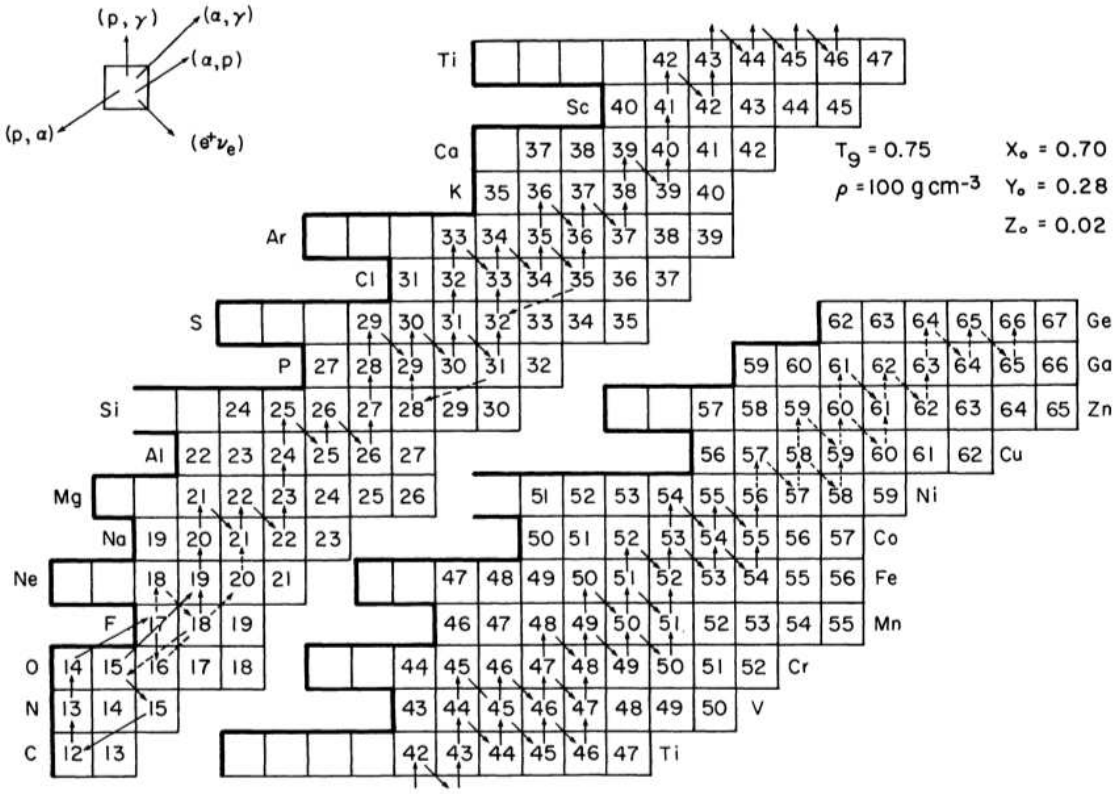

Figure 1.5: An example of the simplified nuclear reaction network at a point of an X-ray burst (Wallace & Woosley 1981). The nuclear evolution was calculated at constant temperature ($T_9 = 0.75$, where T_9 is the temperature in units of 10^9 K or $\approx 10^2$ keV) and density ($\rho = 100$ g cm^{-3}) using a solar mixture of 70% hydrogen, 28% helium, and 2% heavy elements by mass as an initial composition. The number in each box indicates the mass number of each nucleus. Solid and dashed arrows indicate dominant nuclear flows and those roughly an order of magnitude weaker than the solid arrows, respectively.

luminosities and longer durations than those for higher metalicity. In turn, the longer duration of the burst results in a significant extension of the nuclear activity towards the SnSbTe-mass region, which is clearly showed in the mean composition of the envelope at the end of the burst. However, the end products of an X-ray burst is sensitive to the burst history. This means that the burst ashes in the previous bursts significantly affect the composition of the subsequent burst ashes. Thus the nuclear reaction network calculation needs to cover at least several cycles of burst to obtain stable results. This makes it difficult to compare the calculated burst light curves with those of observations. Furthermore, at present we have no observational information on the composition of the burst products. This is very different situation compared to, e,g., nova, for which various observational data are available for the nuclear reaction products. In the case of X-ray bursts, comparison between model calculation and observation is possible only through light curves. This is another reason why the model calculations of X-ray bursts are still under development.

The burst ashes are most likely to be ejected by radiation-driven wind associated with the PRE bursts. Nuclear reaction during the burst is concentrated in the thin layer at the base of the neutron star atmosphere. Because the thermal time scale there is 1–10 sec, while the dynamic time scale is only micro-seconds, the temperature gradient near the burning layer is nearly adiabatic, resulting in a region of highly efficient convection. Weinberg, Bildsten & Schatz (2006) show that the maximum vertical extent of the convective region during the PRE bursts can be sufficiently large that some ashes of burning are ejected by the radiation-driven wind during the PRE phase and are exposed at the neutron star surface following the PRE phase. Woosley et al. (2006) also show convection occurs throughout the burst and the burst ashes are exposed at the NS surface. The ashes on the neutron star surface may form absorption features, which allow us to extract the surface gravitational redshift of the neutron star. If such features could be detected, they can give a direct constrain of the mass-radius ratio.

1.2.4.2 Atmospheric Models

Model calculations of burst spectra have been performed using detailed modeling of the neutron star atmosphere by various authors. In this calculations, hydrostatic and radiative equilibrium in plane-parallel approximation are assumed. The energy spectra of X-ray bursts are generally well represented by a blackbody modified by the circumstellar and interstellar absorptions. However, deviation from a blackbody is commonly observed due to the electron scattering in the hot atmosphere of a neutron star.

When electron scattering becomes significant, emissivity of the source photons is reduced, resulting in the difference between the color temperature and the effective temperature. This has been confirmed by detailed modeling of the neutron star atmosphere (Ebisuzaki 1987; Madej et al. 2004 (MJR04); Majczyna et al. 2005 (MMJR05); Suleimanov et al. 2011 (SPW11)). Figure 1.7 shows the calculated burst spectra emitted from a pure-helium atmosphere with $L/L_{Edd} = 0.95$. Ebisuzaki (1987) showed that the burst spectra are harder than a blackbody spec-

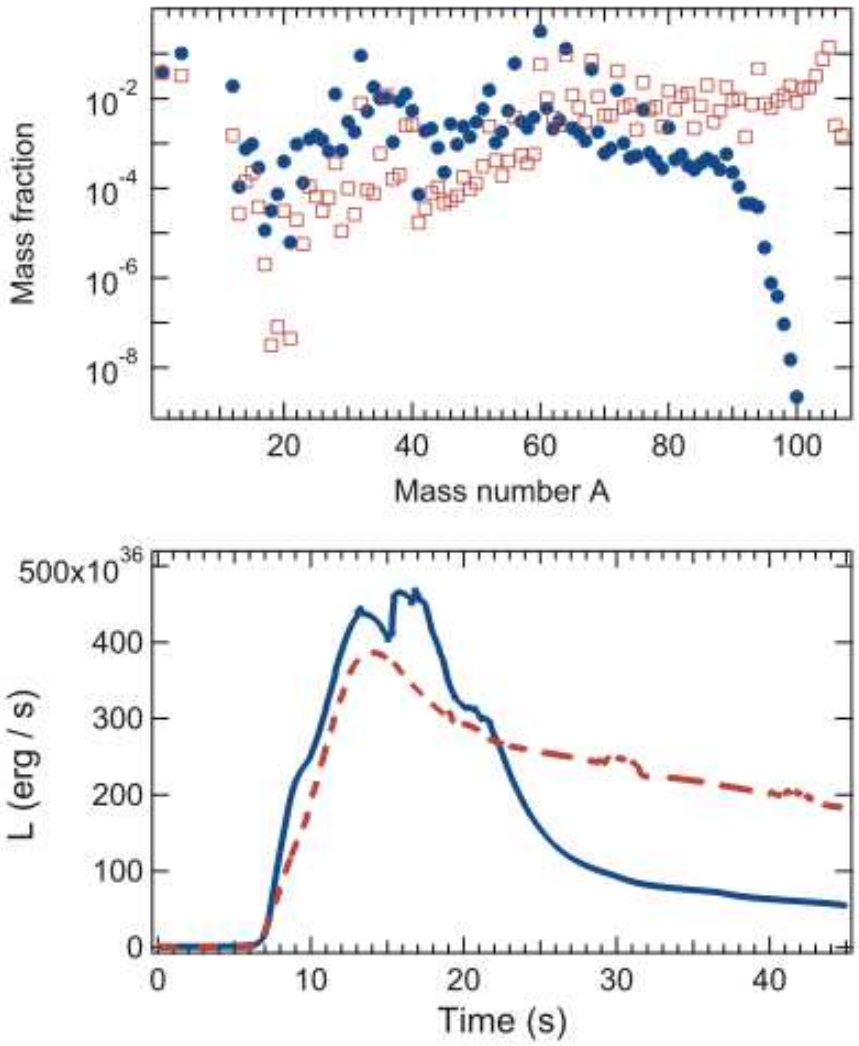

Figure 1.6: Mean composition of the envelope with the different metalicities at a mass accretion rate of $\sim 0.1\dot{M}_{\rm Edd}$ are plotted in the upper panel. Each burst light curve are plotted in the lower panel. Filled circles and the solid line are for accreting solar-like material ($Z = 0.02$), and open squares and the dashed-line are for accreting material of lower metalicity ($Z = 10^{-3}$).

trum at the same effective temperature and can be satisfactorily fitted by a blackbody with a color temperature $T_{\rm c}$ that is higher than the effective temperature $T_{\rm eff}$, although the low-energy excess is often seen below 2 keV. The similar tendencies are also seen in the energy spectra of other models. Such differences are often characterized by the color correction factor, which is defined as $f_{\rm c} = T_{\rm c}/T_{\rm eff}$. Figure 1.8 shows the representative color correction factors obtained for various atmosphere models for bursting neutron stars: Madej et al. (2004) ; Majczyna et al. (2005); Suleimanov et al. (2011). Input parameters of the models are chemical composition, surface gravity, and the luminosity of a neutron star. Different model calculations for the same input parameters generate consistent results with each other at the 2–7 % level.

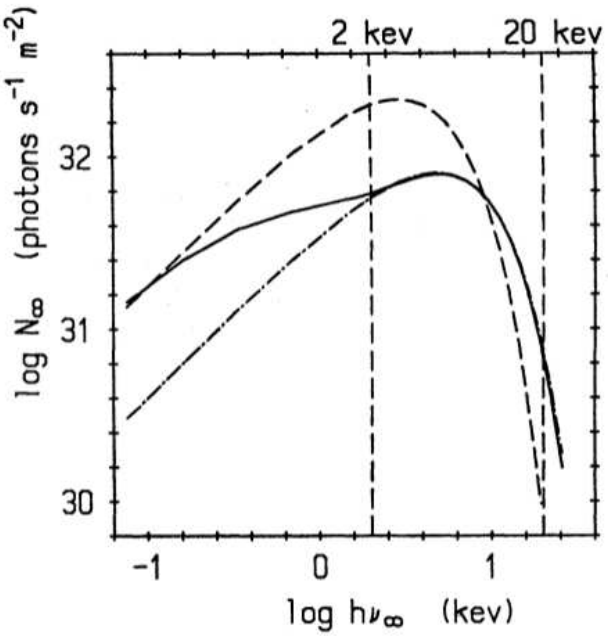

Figure 1.7: The burst spectrum by distant observers with $L/L_{Edd} = 0.95$ (the solid line), which is covered with pure helium matter (Ebisuzaki et al. 1987). The dashed and dot-dashed lines indicate the planckian spectrum at the effective temperature and the fitted planckian spectrum, respectively.

Although simple difference between the color and effective temperature does not distort spectral shape, detailed model calculations show slight deviations from the blackbody spectrum, which depend on various parameters such as luminosities, abundance, etc (Ebisuzaki 1987; Madej et al. 2004; Suleimanov et al. 2012). Especially, Suleimanov et al. (2011) showed an interesting numerical result that, in the low luminosity atmospheres with heavy elements, iron is not completely ionized and its absorption edge appears around $\sim$ 9 keV due to the bound-free transitions from the ground levels of the H-like Fe and He-like Fe. The strength of this edge depends on the metal abundance and the luminosity as demonstrated in figure 1.9. The edge, in reality, should be redshifted due to the strong gravitational field of neutron stars and often smeared due to the rapid spin of neutron stars,

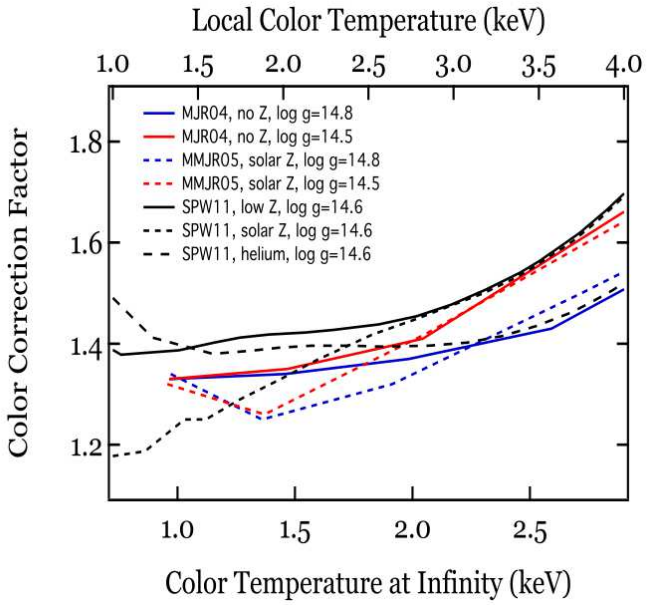

Figure 1.8: A comparison between the color correction factors obtained for atmosphere models for bursting neutron stars for different effective temperatures, surface gravities, and atmospheric compositions (Özel 2013). The models shown are from Madej et al. 2004 (MJR04), Majczyna et al. 2005 (MMJR05), and Suleimanov et al. 2011 (SPW11).

which are not included in the model.

The above models of a neutron star atmosphere in hydrostatic and radiative equilibrium can most likely be applied to an analysis of X-ray burst spectra with small or zero radius expansion. Models by Shaposhnikov & Titarchuk (2002) are applicable to the phases of extremely large radius expansion from an initial 10 km to more than 10,000 km.

1.3 Neutron Stars and the Equation of State of Ultra-Dense Matter

The equation of state (EOS) of ultra-dense matter contains the information on the interior of neutron stars. However, at present, many theoretical EOS models exist reflecting the poor understanding of the nuclear forces, many-body melem, and hadronic correlating at such high densities. Figure 1.10 shows the mass-radius curves of neutron stars by representative EOSs for normal matter such as neutrons and protons, exotic hadronic matter such as hyperons or kaon condensates, and self-bound quark matter, which are collected by Lattimer & Prakash. The allowed mass and radius range of a neutron star are 0.2–2.7 $M_{\odot}$ and 8–15 km, respectively, depending on the assumed models. An accurate measurement of a neutron star mass and radius provides indispensable information to constrain the EOS of ultra-

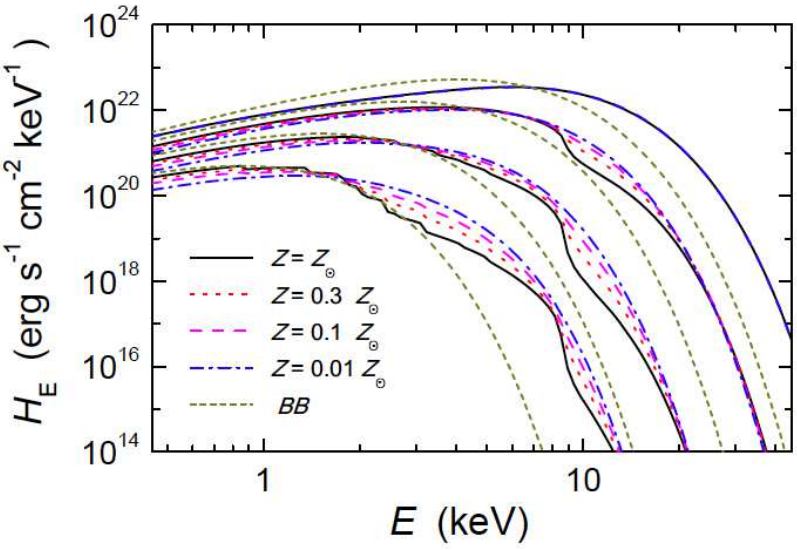

Figure 1.9: Emergent (unredshifted) spectra of the atmosphere models with four relative luminosities ($l = 0.5$, 0.1, 0.01 and 0.001) for solar hydrogen-helium mixture and various abundances of heavy elements: $Z = Z_\odot$ (solid curves), $Z = 0.3\ Z_\odot$ (dotted curves), $Z = 0.1\ Z_\odot$ (dashed curves), $Z = 0.01\ Z_\odot$ (dot-dashed curves) (Suleimanov et al. 2011). The surface gravity is fixed to $\log g = 14.0$. The blackbody spectra with effective temperatures are also shown by short-dashed curves.

dense matter.

Some mass-radius regions of neutron stars are already ruled out by several constraints associated with the compactness limit of neutron stars. The black region in figure 1.10 is ruled out by the general relativity (GR) constraint, which requires the greater radius of a neutron star than the Schwarzschild Radius, $R > 2GM/c^2$, in order not to being a black hole. The dark-grey region is ruled out by finite pressure constraint, which requires $R > (9/4)GM/c^2$ (Lattimer & Prakash 2007). The grey region is by the causality constraint, which requires $R > 2.94GM/c^2$, in order to avoid a supraluminous equation of state in which the speed of sound is faster than the speed of light (see, e.g., Lattimer & Prakash 2007).

The compactness limit is also intimately connected with the rotational limit, when the rotational velocity at the equatorial radius equals to the Keplerian orbital velocity $\Omega = \sqrt{GM/R^3}$, which is given by:

$$\nu_{\rm max} \approx 1.2 \left(\frac{M_{\rm ns}}{1.4 M_\odot} \right)^{1/2} \left(\frac{R_{\rm ns}}{10\ {\rm km}} \right)^{-3/2} {\rm kHz}. \qquad (1.1)$$

At present, the most rapidly rotating pulsar is PSR J1748−2446ad with a spin rate of 716 Hz and its maximum spin rate excluded the right-lower region (light grey), using the above equation. Recently, an 1122 Hz X-ray burst oscillation from XTE J1739-285 has been reported by Kaaret et al. (2006). The stability of this oscillation frequency strongly suggests that it is the spin rate of the neutron star. If true, this may sets relatively stringent limits to constrain the mass-radius

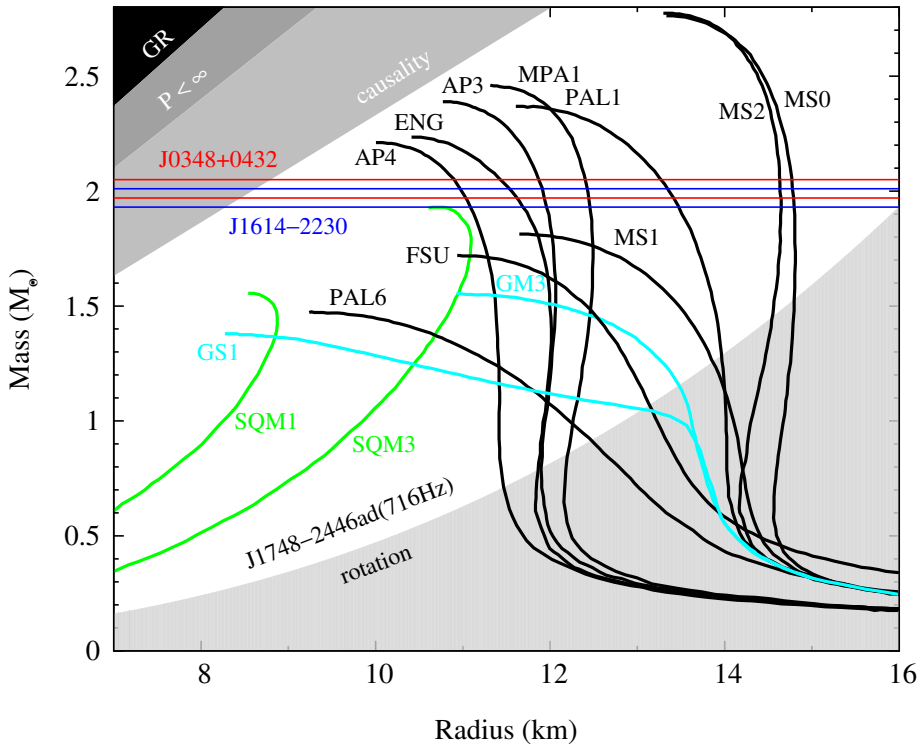

Figure 1.10: Various mass-radius curves of neutron stars for representative EOSs compiled by Lattimer and Prakash (2007), which is adopted form Demorest et al. (2010). The black, cyan, and green curves are for normal matter EOSs, for exotic matter ones, and for self-bound quark matter ones. For normal matter EOSs, ten EOSs can be roughly divided into three groups, according to the calculation approaches: nonrelativistic potential models including AP3-4 (Akmal & Pandharipande 1997), PAL1, and PAL6 (Prakash et al. 1988), relativistic field theoretical models including MS0-2 (Müller & Serot 1996) and FSU (Shen et al. 2011), and relativistic Dirac-Brueckner-Hartree-Fock models including ENG (Engvik et al. 1996) and MPA1 (Müther, Prakash, & Ainsworth 1987). For exotic matter EOSs, GS1 is a relativistic field theoretical model with a condensate of kaons (Glendenning & Schaffner-Bielich 1999) and GM3 is with condensate of hyperons (Glendenning & Moszkowski 1991). For self-bound quark matter EOSs, SQM1 and SQM3 correspond to the different choices of the parameter values (Prakash et al. 1995). The labels of various EOSs follow the notation of Lattimer and Prakash (2001) and details of each EOS model are found in each reference. The left-upper and right-lower region are ruled out by several constraints. See text for details of the constraints. The region between blue and red solid-lines indicate the mass ranges of J1614−2230, $1.97 \pm 0.04 M_{\odot}$, and J0348+0432, $2.01 \pm 0.04 M_{\odot}$, respectively. The EOSs for exotic matter and self-bound quark matter is ruled out by this masses of neutron stars.

relation of neutron stars.

Several recent observations of neutron stars have contributed to the determination of the neutron star masses. Figure 1.11 lists the neutron star masses measured as of January 2014[5]. The measurements include pulsars orbiting another neutron star, a white dwarf or a main-sequence star. The compact nature of several binary pulsars permits detection of relativistic effects, such as Shapiro delay or orbit shrinkage due to gravitational radiation reaction, which constrains the inclination angle and allows the measurement of each mass in the binary. According to this list, the canonical pulsar mass is considered to be ~ 1.4 $M_\odot$. Furthermore, the largest accurately pulsar masses were measured from double neutron stars binary pulsar PSR 1913+16 and their masses are 1.3867 ± 0.0002 and 1.4414 ± 0.0002 $M_\odot$, respectively.

Recently, one significant development concerns the masses measured from two radio binary pulsars with a white dwarf companion: PSR J1614−2230 and PSR J0348+0432. The masses of PSR J1614−2230 and PSR J0348+0432 were measured by the methods of Shapiro delay and radio timing observations phase-resolved optical spectroscopy, respectively. From measurements of PSR J1614+2230, with $M_{\rm ns} = 1.97 \pm 0.04 M_\odot$, and PSR J0348+0432, with $M_{\rm ns} = 2.01 \pm 0.04 M_\odot$, the minimum value of the maximum mass is $M_{\rm ns} = 2M_\odot$. This maximum masses effectively rule out the EOSs for exotic matter and self-bound quark matter, although this is not sufficient to provide critical constraints on the mass-radius relations of neutron stars.

1.4 Methods to Estimate the Mass-Radius Ratios of Neutron Stars

The radius of a neutron star can be measured by observing the thermal emission from the surface of isolated neutron stars or that of neutron stars in LMXBs. However, clear results have not been obtained so far from the above measurements due to large systematic uncertainties, e.g. source distance, color-correction factor, and radiation isotropy. Therefore, instead of directly measuring the radius of a neutron star, it is often measured the mass-radius ratio of a neutron star, i.e. gravitational redshift at the neutron star surface, because it is little affected by systematics among the various methods. This section highlights representative methods to estimate the mass-radius ratio of a neutron star, i.e. the gravitational redshift of a neutron star.

1.4.1 Time Variations of the Eddington Limit

The Eddington limit itself contains information on the mass of a neutron star, but it is difficult to obtain reliable results due to several systematic uncertainties such as source distances and the composition of the neutron star atmospheres.

[5] http://stellarcollapse.org/nsmasses

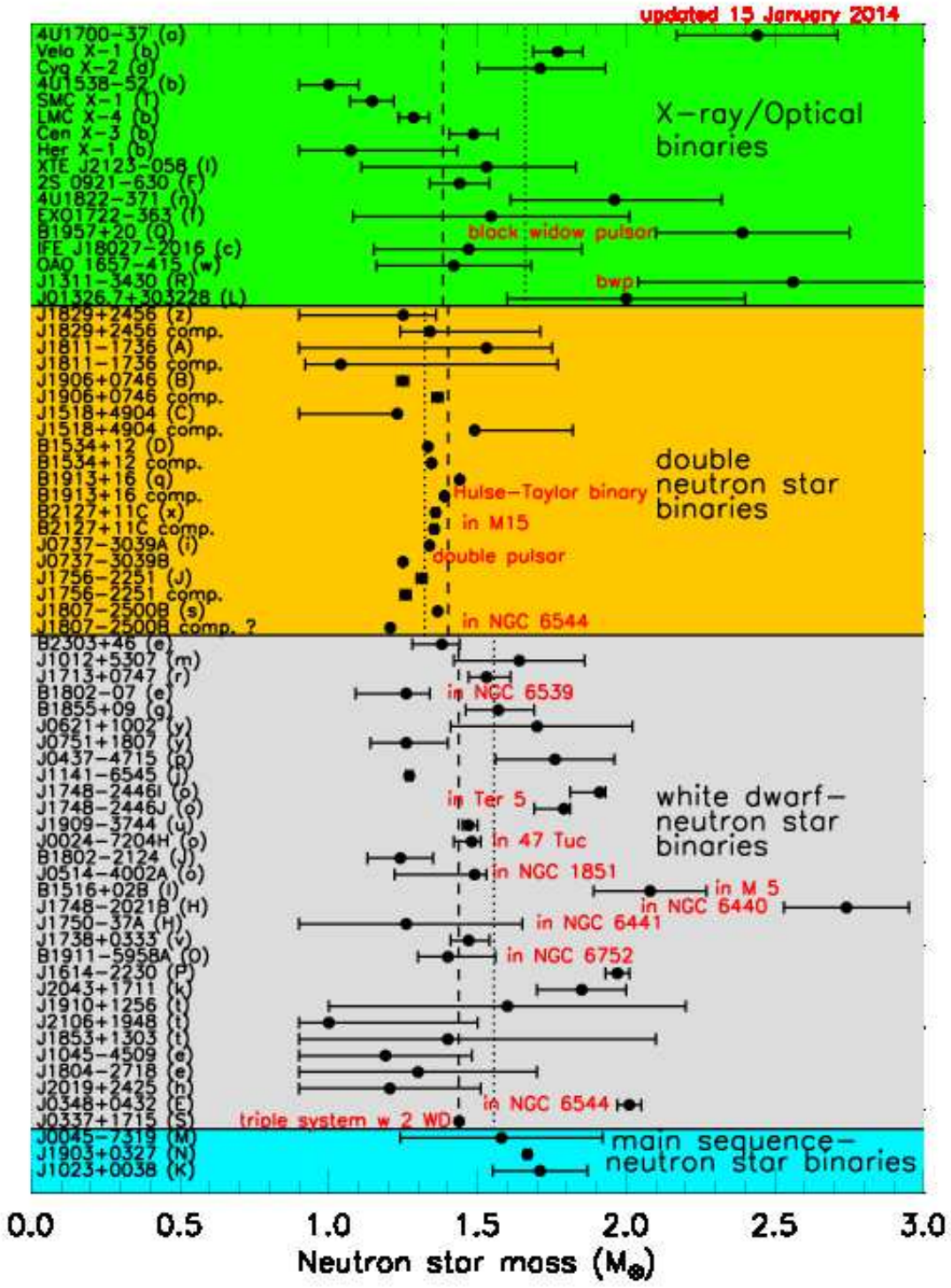

Figure 1.11: A list of the neutron star masses measured as of January 2014, which is reprinted from http://stellarcollapse.org/nsmasses.

Therefore, we focus on a time-variation of the Eddington limit, instead of the Eddington limit itself.

This time-variation is expected to appear in bursts with PRE. In the PRE bursts, the luminosities approaches the Eddington Limit, and its corresponding flux (Eddington limited flux) is given by:

$$\begin{aligned} F_{Edd,\infty}(R) &= \frac{L_{Edd,\infty}(R)}{4\pi d^2 \xi} \\ &= \frac{1}{4\pi d^2 \xi} \frac{4\pi c G M}{\kappa} \sqrt{1 - \frac{2GM}{Rc^2}} = \frac{cGM}{\kappa d^2 \xi} (1+z)^{-1}, \end{aligned} \tag{1.2}$$

where ξ is the anisotropy factor of burst emission and κ is the opacity, given by $\kappa = 0.2(1+X)[1+(\alpha T)^{0.86}]^{-1}$ cm^2 g^{-1}, with X the hydrogen content (by mass) of the neutron star atmosphere, $\alpha = 2.2 \times 10^{-9}$ K^{-1}. During the PRE phase, the luminosity remains constant at Eddington limit, but they are expected to change by a distant observer due to the different gravitational redshift at different photospheric radii. From the time variations of the Eddington luminosities, the gravitational redshift at the neutron star surface is obtained. We classify the case into two according the degree of the PRE.

Firstly, if the PRE is large enough to approximate as the gravitational redshift is $1 + z_{\rm R} \approx 1.0$, the gravitational redshift is, in the simplest method, derived from the ratio of the Eddington fluxes (or Edington luminosities) at very large photospheric radii, where the effect of the gravitational redshift is negligible, and at the moment when the radius expansion has just ended (hereafter "touch-down"). The Eddington limited flux at the very large PRE, where $R \gg R_*$[6], is given by:

$$F_{Edd,\infty} = \frac{L_{Edd,\infty}(R \gg R_*)}{4\pi d^2 \xi} \approx \frac{cGM}{\kappa d^2 \xi}. \tag{1.3}$$

On the other hand, the Eddington limited flux at the touch-down is given by:

$$\begin{aligned} F_{Edd,\infty} &= \frac{L_{Edd,\infty}(R = R_*)}{4\pi d^2 \xi} \\ &= \frac{1}{4\pi d^2 \xi} \frac{4\pi c G M}{\kappa} \sqrt{1 - \frac{2GM}{R_* c^2}} = \frac{cGM}{\kappa d^2 \xi} (1+z_*)^{-1}. \end{aligned} \tag{1.4}$$

By dividing Eq. (1.3) by Eq. (1.4), the gravitational redshift on the neutron star surface is simply derived from the ratio of the observed Eddington limited fluxes, which is given by:

$$1 + z_* \approx \frac{F_{Edd,\infty}(R \gg R_*)}{F_{Edd,\infty}(R = R_*)}. \tag{1.5}$$

It is here assumed that the composition of the neutron star atmospheres does not change and the anisotropic factor of the burst emission remains constant during

[6] In this thesis, the values measured by a local observer on the surface of the star, those by a observer at distance of R from the center of the star, and those by a distant observer is indicated with a subscript $*$, R, and ∞, respectively.

the burst. However, most of the observed PRE bursts do not show large enough PRE to use the above method.

Secondly, if the photospheric radius expansion does not justify the use of a redshift factor of 1.0, the gravitational redshift is derived by using following two ratios. One is the ratio of Eddington limited fluxes during the PRE phase and at the touch-down by a distant observer, which is given by:

$$\zeta_\infty = \frac{F_{Edd,\infty}(R > R_*)}{F_{Edd,\infty}(R = R_*)} = \frac{1+z_*}{1+z_{\rm R}} = \sqrt{\frac{1-\dfrac{R_{\rm s}}{R}}{1-\dfrac{R_{\rm s}}{R_*}}} = \sqrt{\frac{1-\dfrac{1}{\chi}\dfrac{R_{\rm s}}{R_*}}{1-\dfrac{R_{\rm s}}{R_*}}}, \tag{1.6}$$

where the Schwartzschild radius is defined as $R_{\rm s} = 2GM/R_*$ and χ is introduced as the ratio of the photospheric radii during PRE phase to the neutron star radius by an observer on the neutron star surface, which is given by:

$$\chi = \frac{R}{R_*} = \frac{R_\infty}{R_{*,\infty}}\frac{1+z_*}{1+z_{\rm R}} = \chi_\infty \zeta_\infty, \tag{1.7}$$

where χ_∞ is the ratio of above radii by a distant observer. From these two ratios, we obtain the gravitational redshift at the neutron star surface by:

$$1 + z_* = \sqrt{\frac{\zeta_\infty^2 - 1/\chi}{1 - 1/\chi}} = \sqrt{\frac{\zeta_\infty^2 - 1/\chi_\infty\zeta_\infty}{1 - 1/\chi_\infty\zeta_\infty}}. \tag{1.8}$$

Note that, as seen in section 1.2.4, although burst spectra apparently have a Planckian shape, numerical calculations show that the color temperatures $T_{\rm c}$ can differ substantially from the effective temperatures $T_{\rm eff}$. The effect of this can be described by a correction factor $t = T_{\rm c}/T_{\rm eff}$.

In the past studies of X-ray bursts, PRE bursts from 4U 2129+11 with Ginga satellite (van Paradjis et al. 1989) and from EXO 0748−676, 4U 1636−536, 4U 1735−44, and 4U 1820−30 with EXOSAT satellites (Damen et al. 1990) were used to apply the time-variation of the Eddington limit to estimate the gravitational redshifts. These values suffers from various systematic errors and thus did not provide a significant constrain on the mass-radius relations.

1.4.2 Absorption Features

Absorption features at the neutron star surface can be used to measure the gravitational redshifts. The absorption features, i.e. the absorption lines or edges, may be redshifted to the observed line/edge energies, $E_{\rm obs}$, from those in laboratory, E_0, by the general relativistic effect due to the strong gravitational fields of neutron stars. From this redshifted energy, one can get the gravitational shift, which is given by:

$$\frac{E_0}{E_{\rm obs}} = 1 + z = \left(1 - \frac{2GM}{Rc^2}\right)^{-1/2}. \tag{1.9}$$

If absorption features were detected in the energy spectra, the gravitational redshift can be derived immediately from the above equation, once the ions responsible for the features are identified. Although the identification of the ions is difficult, the method is hardly affected by the systematic errors, e.g. the source distance, continuum models, radiation isotropy, and this is expected to give the clear and clean results separated from the above uncertainties.

The spectral features at the neutron star surface may be smeared by two major effects. One is the rotational broadening due to the rapid spin of a neutron star. For the neutron stars with the rapid spin frequencies, the structures on the neutron star surfaces such as absorption line/edge should be modified by rotational broadening, $\Delta E_{\rm rot}$, (Chang et al. 2005; Özel 2013), which is given by:

$$\Delta E_{\rm rot} \simeq 240 \left(\frac{\nu_{\rm spin}}{600\ {\rm Hz}} \right) \left(\frac{R}{10\ {\rm km}} \right) \left(\frac{E_{\rm tran}}{1\ {\rm keV}} \right) \sin i\ {\rm eV}, \tag{1.10}$$

where $\nu_{\rm spin}$ is the spin frequencie of a neutron star, $E_{\rm tran}$ is the energy of the transition, and i is the disk inclination. The other is the Zeeman splitting due to the magnetic field of neutron stars. The magnetic fields in the line-forming region broaden the absorption line/edge with a scale given by:

$$\Delta E \approx 12 \left(\frac{\rm B}{10^9\ {\rm G}} \right)\ {\rm eV}, \tag{1.11}$$

where B is the magnetic field strength at the neutron star surface (Loeb 2003). Otherwise, there are also thermal Doppler broadening and Stark (pressure) broadening, but these influences is small, a few eV, compared to the above major effects and can be ignored. The major effects make the detection of the adsorption line/edge difficult. Therefore, one must carefully select the targets to detect such features or, if the adsorption features are smeared, the analysis in consideration of the effects is required.

Detections of the absorption lines in the burst spectra was reported by several authors. The 4.1 keV absorption lines were detected in the bursts from 4U 1636–536 and 4U 1068–52 with Tenma (Waki et al. 1984; Nakamura et al. 1988) and from EXO 1747–214 with EXOSAT (Magnier et al. 1989). However, these lines were not detected in the subsequent observations. Detection of absorption lines corresponding to the L_α transition of hydrogen-like and helium-like Fe were claimed from EXO 0748–676 using XMM-Newton Reflection Grating Spectrometer by Cottam, Parels, & Méndez (2002). However, the absorption lines were not confirmed with much longer exposure of data (Cottam et al. 2008). Therefore, presence of the absorption lines in the burst spectra is not established yet.

1.4.3 Pulse Profile

The amplitude and the shape of a phase-folded burst oscillation light curve can be very useful to obtain simultaneously the mass and radius of neutron stars. The phase-folded light curves are affected by two effects: gravitational bending of light and Doppler boosting. Gravitational bending of light allows an observer to see

much more than the facing hemisphere. The light bending causes the variations of the amplitude of the phase-folded light curve, depending on the compactness of the neutron star. The Doppler boosting, i.e. spin-related surface speed, also causes the transformation of the intensity of the phase-folded light curves, depending on the radii of neutron stars. Therefore, when combined with these result, the mass and radius of a neutron star is simultaneously obtained from the above analysis. For example, this method was applied to several burst oscillations from 4U 1636−536 (Nath et al. 2002) and from XTE J1814−338 (Bhattacharyya et al. 2005). However, the large uncertainties in the mass-radius measurements influence the various geometric factors, which are difficult to constrain. However, this method is largely affected by various geometric uncertainties and no significant result has been obtained so far.

The above method is also applied to pulsation in the X-ray thermal emission from millisecond pulsars. The pulsation frequency is consistent with the spin frequency of the neutron star, because such pulsations are caused by the periodic motion of a hot spot due to the stellar spin. These pulsations are more coherent than burst oscillations, enabling to accumulate data for a long time. On the other hand, the burst oscillation frequency evolve appreciably in a short time. Therefore, the millisecond pulsar pulsation method gives a more accurate measurement than the burst oscillation method. One of the examples to which this method is applied is the nearest known millisecond pulsar PSR J0437−4715 in ROSAT, Chandra, and XMM-Newton X-ray observations. However, no significant result was obtained due to the known cross-calibration uncertainties of the various detectors and the inadequate absolute timing precision between the detectors. At present, further improvements in mass-radius measurements of millisecond pulsars are hindered by the instrumental limitations of existing X-ray satellites. Indeed, this has served as one of the principal science drivers for the Neutron Star Interior Composition ExploreR (NICER) X-ray timing instrument, which is currently scheduled for launch in late 2016. Its scientific payload is a non-imaging X-ray timing instrument and silicon drift detector pairs. Its unique capability of large effective area (nearly 2000 cm^2 at 1.5 keV) and high precision timing capabilities (100 ns absolute time resolution) can serve as the above millisecond pulsar pulsation method. Details of NICER and its instruments are found in Gendreau et al. (2012).

1.5 Aims of the Current Thesis

A main aim of this thesis is to constrain the mass-radius relation of neutron stars from the X-ray observation. At present, it is difficult to measure the radius of a neutron star accurately, because the nature of the neutron star atmosphere is poorly known. Instead, in this thesis, we evaluate the mass-radius ratio, i.e. gravitational redshift at the neutron star surface, utilizing an absorption feature in the energy spectrum from the surface of a neutron star. The energy of the absorption feature can be determined accurately as it is little affected by systematics. An absorption feature is in principal observable during the thermonuclear X-ray bursts,

especially those with photospheric-radius expansion. If absorption features are detected in the emission from the photosphere of a neutron star, they can directly indicate the gravitational redshift, resulting in a constraint of the mass-radius relations of neutron stars.

This thesis is organized as follows. Chapter 2 describes the Suzaku satellite and the selection of thermonuclear X-ray bursts with its archival data. Details of the spectral analysis during the selected X-ray bursts are presented in Chapter 3. In Chapter 4, the results are discussed and conclusions are summarized.

Chapter 2

X-ray Bursts Observed with Suzaku

We used the Suzaku archive data for the present analysis. Therefore, we will first overview the Suzaku satellite and its instruments, and then systematic analysis of the Suzaku archive data to look for the thermonuclear X-ray bursts, especially those with PRE.

2.1 The Suzaku Satellite

2.1.1 Overview of Suzaku

Suzaku is the Japanese fifth X-ray astronomy satellite and was developed at the Institute of Space and Astronautical Science (ISAS/JAXA) in collaboration with Goddard Space Flight Center (GSFC/NASA) and so on. It was launched on July, 2005, and was successfully put into a near-circular orbit at an altitude of $\simeq$ 570 km and inclination of 32 degrees. Figure 2.1 and figure 2.2 show a schematic side view of Suzaku and its cross-section view, respectively.

Suzaku covers the energy range 0.2–600 keV and is equipped with two types of instruments. One is X-ray Imaging Spectrometer (XIS: Koyama et al. 2007) and each XIS is located at the focal plane of a dedicated X-ray telescope (XRT: Serlemitsos et al. 2007). The other is Hard X-ray Detector (HXD) that is a non-imaging detector covering 10–600 keV (Takahashi et al. 2007; Kokubun et al. 2007). As the HXD data was not used in this thesis, I do not describe it further. Suzaku also carries a third instrument, an X-ray micro-calorimeter (X-ray Spectrometer; XRS), but the XRS is not operational due to sudden loss of its cryogen just after the launch. In the following sections, I first overview XRT and XIS, and then introduce briefly the software needed for the analysis of the Suzaku data.

2.1.2 X-ray telescope (XRT)

XRT consists of 5 sets of the X-ray telescope that is a thin-foil-nested Wolter-I type telescope. Four of them are used for XIS (XRT-I0 through XRT-I3) and its focal length is 4.75 m. One of them is also used for XRS (XRT-S). The angular

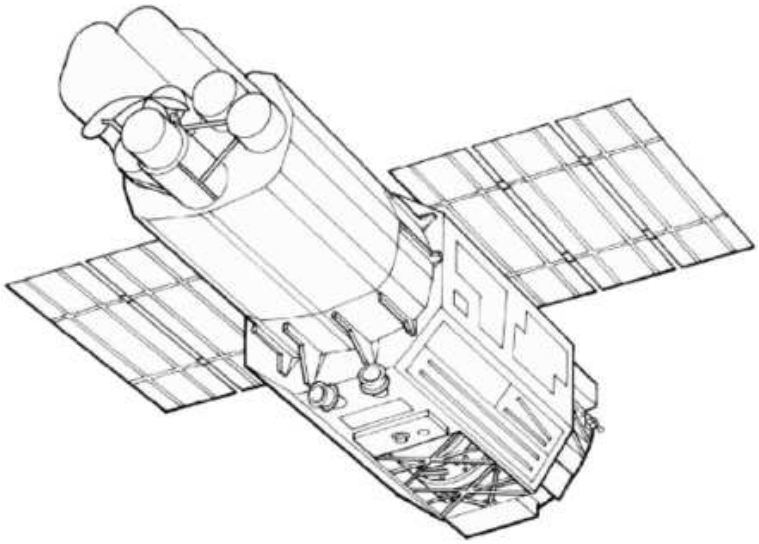

Figure 2.1: Schematic view of the Suzaku satellite in orbit (Mitsuda et al. 2007). Both solar paddles and the extensible optical bench are deployed.

resolution of the XRTs range from 1.8′ to 2.3′, expressed in terms of the half-power diameter (HPD), which is the diameter within which half of the focused X-ray is enclosed. The angular resolutions of XRT does not significantly depend on the energy of incident photons between 0.2–10 keV, which is the energy range of XIS. Figure 2.3 shows the total effective area of 4 XRT-Is in comparison with those of other working satellites. The effective areas of XRT-Is are typically 440 cm^2 at 1.5 keV and 250 cm^2 at 8 keV per telescope. The effective areas are much larger than that of Chandra and comparable to XMM-Newton above 5 keV.

Figure 2.4 shows the encircled energy function (EEF) of a typical quadrant of XRT-I at three energies (4.51 keV, 8.04 keV, and 9.44 keV). The EEF is an integrated value of the point spread function (PSF) with radius, which indicates the normalized intensity distribution of the image of a point source, is integrated. The HPD of XRT-I0 ($\sim 1.9'$), which is twice as large as the diameter at which the EEF becomes half of the normalized effective area, was significantly improved from that of ASCA ($\sim 3.6'$). The HPD at the three energies are nearly identical, being slightly smaller at the highest energy of 9.44 keV. These values are generally consistent with those expected from ground-based calibration measurements.

2.1.3 X-ray Imaging Spectrometer (XIS)

XIS consists of 4 sets of identical CCD cameras that are operated in a photon-counting mode. CCD cameras are sensitive in 0.2–12.0 keV and its energy resolution is $\sim$ 130 eV at 6 keV (full width at half maximum; FWHM). Three of them are equipped with a front-side illuminated CCD (FI-CCD: XIS 0, 2 and 3) and one of them with a back-side illuminated CCD (BI-CCD: XIS 1). Figure 2.6 shows the quantum efficiency (QE) curve of both the FI-CCDs and the BI CCD. The BI-CCD has better QE than the FI-CCD in the soft band because there is

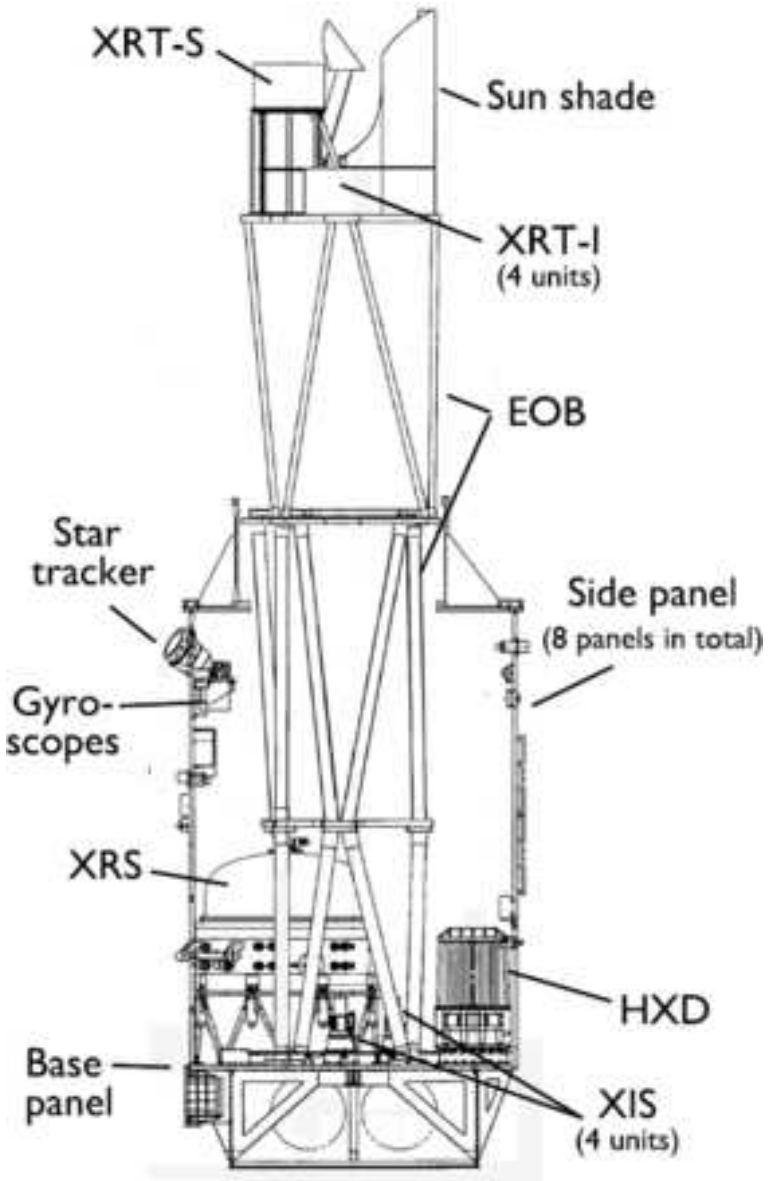

Figure 2.2: A schematic cross-section view of Suzaku with the optical bench extended showing the internal structures (Mitsuda et al. 2007).

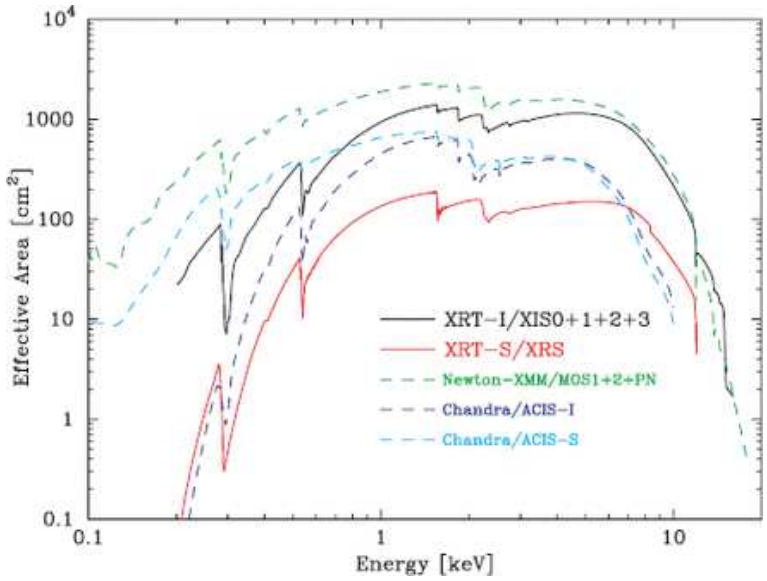

Figure 2.3: Total effective area of the four XRT-I modules (Serlemitsos et al. 2007). These are compared with that of XMM-Newton and Chandra. Transmissions of the thermal shield and the optical blocking filter, and the quantum efficiency of the CCD camera are all taken into account.

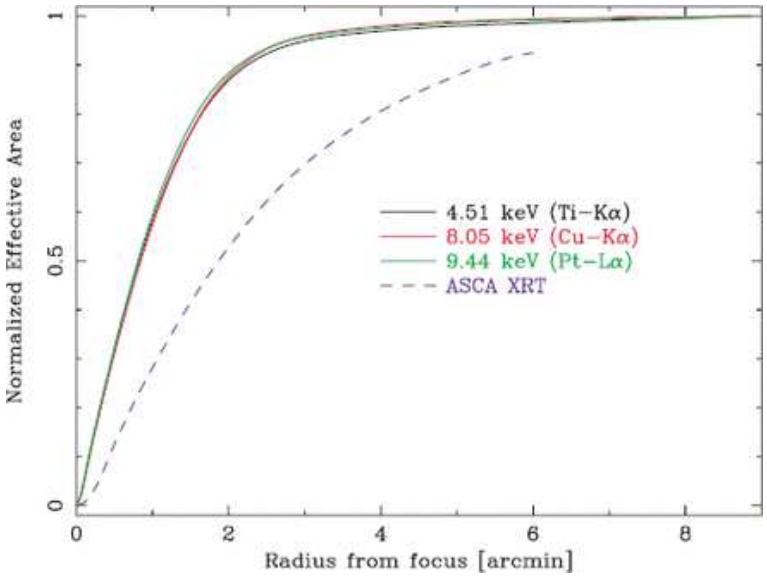

Figure 2.4: Encircled-energy fraction (EEF) of a typical quadrant of XRT-I at different energies: 4.51keV, 8.04keV, and 9.44keV (Serlemitsos et al. 2007). These EEF are compared with that of ASCA measured at 4.51keV. The diameter used to define the 100% flux as 24′ for the ASCA XRT and 17.8′, which is same as the size of CCD camera for the XRT-I quadrant.

no gate structures at the incident surface of photons, but has lower QE in the hard band due to a thinner depletion layer of ~ 42 μm than those of the FI-CCDs (~ 65 μm). The imaging area of each CCD has 1024×1024 pixels with a pixel size of 24×24 μm. When combined with the XRT, the XIS field of view is $18' \times 18'$ and spatial resolutions of XIS becomes 2 arcmin (FWHM). Figure 2.5 shows the schematic view of an XIS. Each CCD camera has a single CCD chip, which consists of the imaging area and the frame store area. The imaging area is exposed to the sky for observations, while the frame store area is shielded throughout observations. Each CCD camera is divided into 4 segments, which is called segment A, B, C, and D. The data in each segment are read out from a dedicated node and are sent to the common telemetry of a CCD camera.

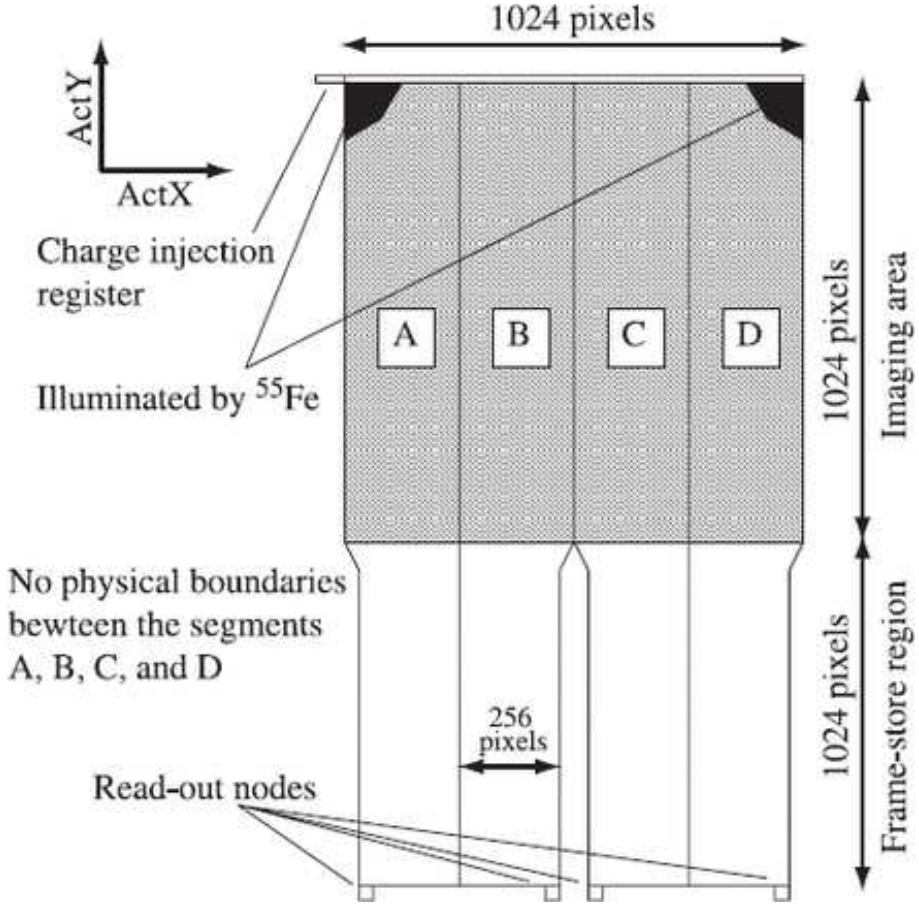

Figure 2.5: Schematic view of a XIS (Koyama et al. 2007). The CCD consists of 4 segments (A, B, C, and D), each with a dedicated read-out node.

In XIS, we use most often normal mode, which is one of two major clocking modes, to operate the CCDs and furthermore it can be combined with several options. In general, CCDs are read out every 8 sec in the normal mode, thus affording data with the exposure time and the time resolution of 8 sec. Another major types of clocking mode is P-sum mode that is for stacked readout, but we do not describe it further because it was not used in this thesis.

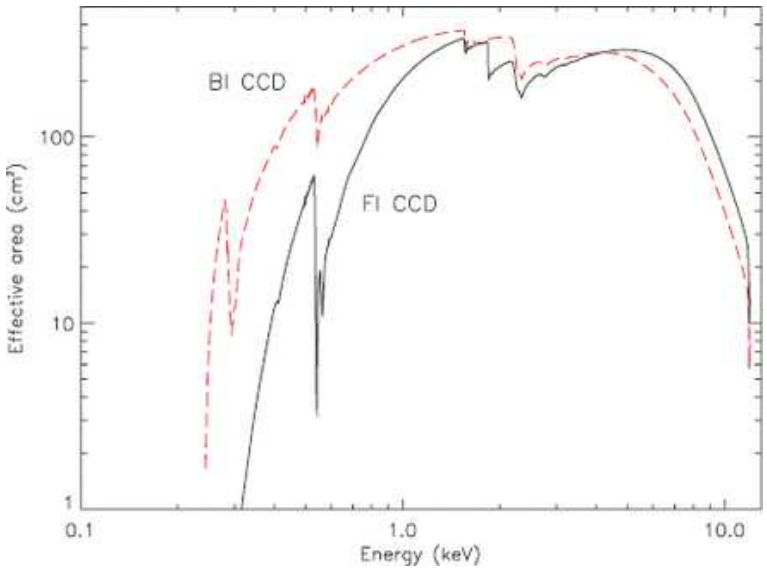

Figure 2.6: The QE as a function of incident energy, calculated using best estimate values of the thickness of dead layers and depletion layer (Koyama et al. 2007). The solid line represents the FI-CCD (XIS 0) and the broken line is for the BI-CCD (XIS 1).

When observing a bright source, the large count rate sometimes causes the photon pile-up and/or the telemetry saturation. The XIS has a quota for the telemetry per unit time, which depends on the observation mode and the data rate. If the telemetry exceeds its quota, a part of the telemetry is lost. Photon pile-up occurs when multiple photons arrive at a pixel or adjacent pixels within the frame time. If two photons with energies $E1$ and $E2$ arrive, they are mistakenly recognized as a single photon with an energy of $E1 + E2$. It is known that this modifies the grade branching ratios, energy spectra, light curves, and the images in X-ray CCD instruments. Specifically, the following observational features appear:

- If the flux changes during an observation, a plateau phase often appear at the peak of the piled-up light curve.
- A decrease of the fraction of single-pixel events (grade 0) and an increase of multiple-pixel events (grade 2, 3, 4, and 6) appear in the grade branching ratio of the piled-up data. Fraction of non-X-ray events (grade 1 and 7) also increase.
- A relative reduction of the soft X-ray events and a relative increase of hard X-ray events occur in a piled-up spectrum. As a result, a hard tail is artificially created in the spectrum.

Significance of these effects depends on the incident flux and its spectral shape. Details of pile-up effects on the XIS are found in Yamada et al. (2012).

The above-mentioned problems are mitigated by two options: one is a window option and the other is a burst option. The window and burst option are partially

read out in time and space, respectively. In the $1/w$ window option, the central $1024/w$ pixels are read out in the Y direction and the entire pixels are read out in the X direction, yielding a $1024 \times 1024/w$ pixel image. The exposure time is $8/w$ sec. In the b sec burst option, all pixels are read out, but the effective exposure time is reduced to b sec ($b < 8$ sec). The events detected during $8 - b$ sec of exposure time are transferred and discarded without being recorded. Events detected in the remaining b sec are transferred and recorded. In $1/w$ window and b sec burst mode, the central $1024 \times 1024/w$ pixel image is read out with an exposure time of b sec. During the exposure time, events in the first $8/w - b$ sec are discarded and those in the last b sec are recorded. The inequity of $8/w > b$ always holds.

2.1.4 Software for the analysis of Suzaku data

For the analysis of Suzaku data, two major types of software are needed: one is the multi-mission collection of programs and scripts (HEAsoft) and the other is the relevant calibration database (CALDB). In what follows, we used the Suzaku data processed by HEAsoft version 2.4b and CALDB released on July 1, 2014.

2.2 X-ray Bursts Observed with Suzaku

We used the Suzaku archive data to look for X-ray bursts. Some bursts were detected in the observations whose target was an X-ray burst source, and others were detected by chance in the observations whose target was not a known burst source. In this thesis, we firstly looked in the data from the bursts when Suzaku pointed to the X-ray burst sources, referring a catalogue of thermonuclear X-ray burst sources in the Galaxy[1]. Table 2.1 lists the X-ray bursts sources observed with Suzaku (as of September 2015), which includes 70 observations of 28 different burst sources. We then made light curves of each data, in order to search for X-ray bursts. If an X-ray burst occurs, a light curve clearly shows a sudden increase of the flux by orders of magnitude. Looking at the light curves by eye, 44 X-ray bursts were found from 9 different burst sources: EXO 0748−676, 4U 1608−522, 4U 1636−536, 4U 1705−44, XTE J1710−281, 4U 1728−34, GRS 1747−312, GX 17+2, and Aql X-1.

To check whether the above X-ray bursts show PRE, I calculated the light curves in two different energy bands: low- (0.5–4 keV) and high- (4–10 keV) energy bands. When an X-ray burst shows PRE, the radius of the photosphere increases largely and the temperature decreases significantly below ~ 2 keV, a typical peak temperature of bursts without PRE. This causes an increase of low-energy flux and a decrease of high-energy flux. Therefore, a PRE burst shows a characteristic light curve with a dip of high-energy flux and a dominant low-energy flux. Our analysis of the above 44 X-ray bursts showed a hint of a PRE burst from GRS 1747−312. Note that I here ignored short PRE bursts, whose duration of the PRE phase is less than 8 sec, because they do not have enough statistics to look for the spectral features in the energy spectra.

[1] https://personal.sron.nl/∼jeanz/bursterlist.html

Table 2.1: Thermonuclear X-ray bursts observed with Suzaku

Source	R.A.	Decl.	n_{obs}	n_{burst}	n_{pre}
4U 0614+09	94.28042	9.136944	2	...	...
EXO 0748−676	117.1408	−67.7525	1	5	...
4U 1323−62	201.6504	−62.13611	1	...	...
Cen X-4	224.5917	−31.66889	1	...	...
Cir X-1	230.1704	−57.16694	1	...	...
4U 1608−522	243.1792	−52.42306	4	3	...
4U 1636−536	250.2312	−53.75139	5	10	...
4U 1705−44	257.227	−44.10205	8	7	...
XTE J1710−281	257.5512	−28.13167	1	4	...
4U 1728−34	262.9892	−33.83472	1	2	...
SLX 1737−282	265.1625	−28.29667	1	...	...
KS 1741−293	266.2333	−29.35194	2	...	...
AX J1745.6−2901	266.4008	−29.02611	1	...	...
1A 1742−294	266.5229	−29.51528	3	...	...
SLX 1744−300	266.8558	−30.04472	1	...	...
GRS 1747−312	267.6896	−31.2922	1	1	1
SAX J1808.4−3658	272.1147	−36.97897	1	...	...
XTE J1810−189	272.5862	−19.06972	1	...	...
4U 1812−12	273.7758	−12.09642	1	...	...
GX 17+2	274.0058	−14.0639	3	1	...
4U 1820−303	275.9187	−30.36114	8	...	...
GS 1826−24	277.3675	−23.79139	1	...	...
Ser X-1	279.9896	5.035833	4	...	...
HETE J1900.1−2455	285.0407	−24.90119	1	...	...
Aql X-1	287.8167	0.585	10	11	...
XB 1916−053	289.6991	−5.236444	3	...	...
Swift J1922.7−1716	290.654	−17.284	1	...	...
Cyg X-2	326.1717	38.32167	2	...	...
Total (28 sources)			70	44	1

GRS 1747−312 was observed with Suzaku as a part of Galactic bulge mapping observations in September, 2009, for a total exposure of 45.3 ks. Suzaku happened to cover GRS 1747−312, a LMXB located in the globular cluster Terzan 6 (Predehl et al. 1991; Pavlinsky et al. 1994). Distance to the globular cluster is estimated to be $9.5^{+3.3}_{-2.5}$ kpc (Kuulkers et al. 2003). The source is also known to show dips and eclipses (in't Zand et al. 2003a) with an orbital period of 12.36 hr. The long orbital period suggests that the companion star may be a subgiant star, but should not be a white dwarf. Thus the accreted matter from the companion star is likely to be hydrogen-rich. It produces outbursts every 4–5 months, each of which lasts $\sim$ 1 month (in't Zand et al. 2000; 2003a). Two successive outbursts were observed with RXTE in 2001. X-ray bursts detected with RXTE during the outbursts were described in in't Zand et al. (2003a), including those with PRE. We note that their data might be contaminated with some other burst sources in the RXTE field of views during the observations, because GRS 1747−312 is located near the Galactic center and RXTE is equipped with non-imaging detectors with relatively wide field of view (1 deg in FWHM). See Galloway et al. (2008) for further information. In this thesis, we concentrate on the burst data from GRS 1747−312. The analysis of the persistent emission is presented in Saji et al. (2015).

Chapter 3

Analysis & Results of the PRE Burst from GRS 1747–312

With the first look at the archive data, it was apparent that a bright point source dominated the XIS image. Furthermore, an X-ray burst was detected from the source. We determined the location of the point source using the data during the burst as $(\alpha, \delta) = (267.699, -31.271)$ (J2000), whose error radius is estimated to be 19 arcsec (Uchiyama et al. 2008). This position is consistent with that determined based on the persistent emission (Saji et al. 2015). GRS 1747−312 is the only known bright X-ray source in the error circle (See in't Zand et al. (2003a) for the Chandra position of GRS 1747−312). Thus, we interpret the bright source in the XIS image as GRS 1747−312. However, we cannot exclude the possibility that the bright source is another contaminant source, which is not known so far, in the globular cluster Terzan 6, as the estimated core radius of Terzan 6, ~ 3 arcsec, is smaller than the angular resolution of the Suzaku satellite, ~ 6 arcsec. Detailed discussion on the source identification is found in Saji et al. (2015). Because we cannot exclude the possibility of the source confusion, we need to note the parameters of GRS 1747−312, e.g., orbital inclination, in the data analysis. For the following analysis of the data, we extracted the source photons from a circular region with the radius of 4.3 arcmin centered at the image peak.

Figure 3.1 shows a light curve obtained with XIS 0 for the 0.5–10 keV band. A long X-ray burst, which is indicated by an arrow, was detected from GRS 1747−312. The data from the time-region A is used to subtract the persistent emission from the burst data. Saji et al. (2015) shows that the spectrum of the persistent emission during the observation with Suzaku are well-reproduced by two models: Comptonized emission plus blackbody model and Comptonized emission model modified by a partial-covering absorption model. The flux of persistent emission is $\sim 1.2 \times 10^{35}$ erg s^{-1}, assuming that the distance to the source is the same as that to the host globular cluster of 9.5 kpc. Figure 3.2 shows the close-up light curves of the burst with the minimum time resolution in the same energy band as in figure 3.1. The burst has a relatively long duration of the e-folding time of 117 ± 6 sec, compared with that of typical X-ray bursts. The burst after 192 sec from the burst onset in figure 3.1) was not observed due to the satellite passage through the South Atlantic Anomaly (SAA).

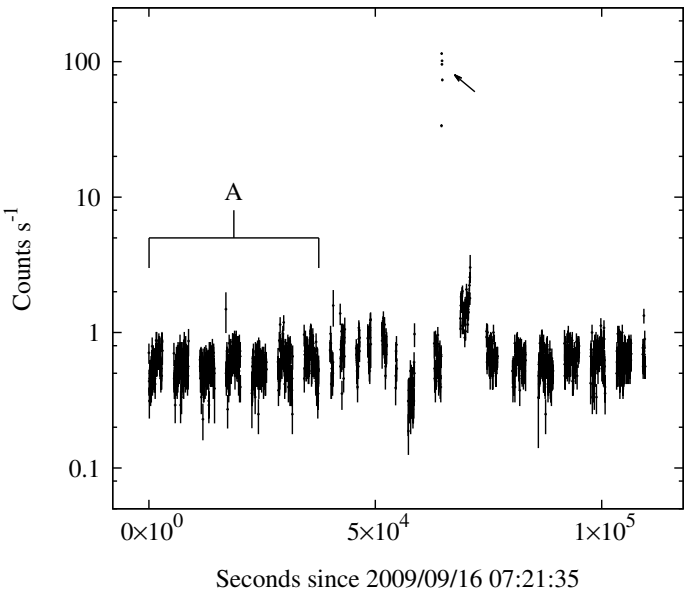

Figure 3.1: An XIS 0 light curve of GRS 1747−312 in the 0.5–10 keV band with 192-sec time bins. An X-ray burst is indicated by an arrow. The data from the time-region A is used to subtract the persistent emission from the burst data.

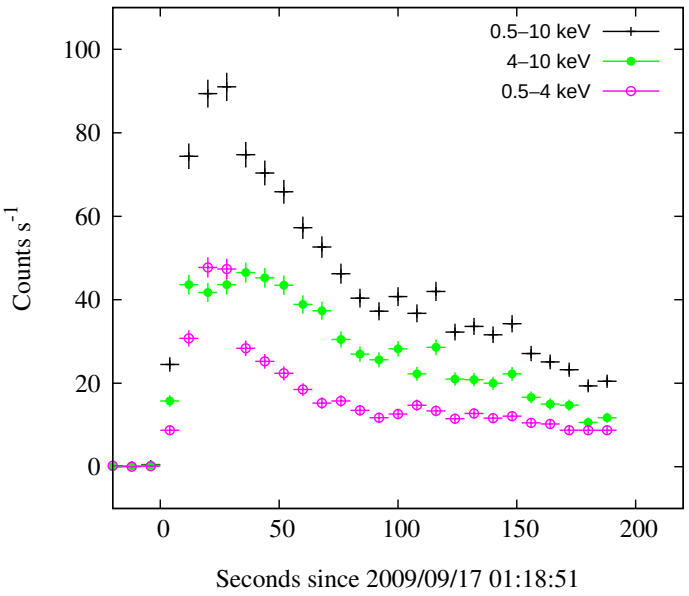

Figure 3.2: An XIS 0 close-up light curves during and immediately before the X-ray burst. The crosses (black), filled circles (green), and open circles (magenta) indicate the light curves in the all (0.5–10 keV), high- (4–10 keV), and low- (0.5–4 keV) energy bands, respectively. No datum was obtained after 192 sec from the burst onset due to the SAA passage of the satellite. Only the segment B data are used to describe the light curves because of the telemetry saturation of the XIS 0 data.

3.1 Data Selection

In analyzing the burst data, the photon pile-up and the telemetry saturation both due to the large count rate must be carefully addressed. Significance of the pile-up is apparent in the present burst data from the change of grade branching ratio (especially the increase in grade 1 events) and from the count rate itself. We decided to exclude the center region of the image referring to the technical description of Suzaku[1]. When an energy spectrum is affected by the photon pile-up, a hard tail is artificially created in the spectrum. If the center region of the image is appropriately excluded, the hard tail will disappear. Then, because the effects of photon pile-up is negligible in the outer region of 2.15–4.3 arcmin, we was usable a region where the spectrum does not show the hard tail compared with that in the outer region. As a result, we found that, if we exclude a circular region of 1.4 arcmin in radius centered at the image throughout the burst, the effects of the photon pile-up become insignificant. Thus, we used the source photons extracted only from the annular region of 1.4–4.3 arcmin in radius for the analysis of the burst data.

In addition, we checked the telemetry saturation for each time bin of data for each CCD. In the cases of XIS 0 and 3, telemetry saturation resulted in the event loss in the data in segments A, C, and D, whereas no event loss was found in segment B, because segment B outputs the data to telemetry first among the 4 segments. Hence, we used the segment B data only during the period of telemetry saturation in XIS 0 and 3 (8–128 sec from the burst onset). This means that source photons are extracted from the overlap of segment B and the annular region. The Ancillary Response File (ARF) is also created for the overlapping region. For XIS 1, we used the segment B data only during the period of mild telemetry saturation of 112–136 sec from the burst onset, and the data of all the segments after 136 sec. However, no data at all was usable, including segment B, for 8–112 sec because the telemetry saturation was too severe. In calculating the source flux, we corrected for the loss of the effective area, using the ARF.

3.2 Properties of the X-ray Burst

To see the properties of the X-ray burst, we estimated the burst parameters and their time-variations. We derived energy spectra of the burst every 8 sec in 1–10 keV. In this analysis, we have discarded the data below 1 keV, where very few source photons are available due to large interstellar absorption. For this purpose, we used only the FI-CCD data because the BI-CCD data suffer from heavy telemetry saturation (see section 3.1). Note that BI-CCD data are used for the detailed spectral analysis later. We extracted the spectra in the time-region A (figure 3.1) prior to the burst as the template for the persistent emission, subtracted their average from the energy spectra during the burst. Although the persistent emission level may have somewhat changed during the burst, it should hardly affect this results because the flux during the burst is larger at least by

[1]http://www.astro.isas.jaxa.jp/suzaku/doc/suzaku_td

two orders of magnitude than that in the persistent phase. We then fitted the spectrum in each time bin with an absorbed blackbody model (phabs × bbody in the notation of XSPEC, the X-ray spectral fitting package, Arnaud 1996). The spectrum in each time bin is showed in the Appendix B. Figure 3.3 plots the resultant time-evolutions of the major parameters: bolometric luminosity, color-temperature, apparent radius, hydrogen column density, and reduced chi-square, whose degrees of freedom range between 18 and 24, from the top to bottom panels. Note that we assumed here and after that the distance to the source is the same as that to the host globular cluster of 9.5 kpc.

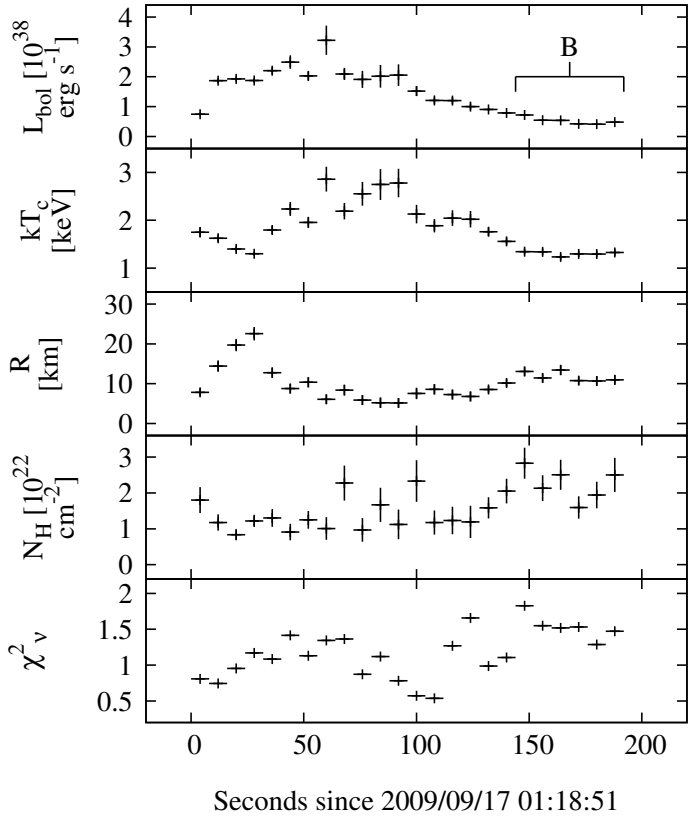

Figure 3.3: Time-evolutions of the best-fit spectral parameters during the burst: a bolometric luminosity, a color-temperature, an apparent radius, a hydrogen column density, and a reduced chi-square, from top to bottom. The source distance is assumed to be 9.5 kpc. The horizontal bars of the data points represent integration time (8 sec) of the data, and the vertical bars errors in the 90% confidence limit. Time-region B is used in detailed analysis of the spectral feature (section 3.3).

The third panel of figure 3.3 clearly demonstrates that the moderate PRE occurred in the initial 80 sec after the burst onset. The apparent radius shows moderate increase by a factor of ~ 4 in the initial ~ 30 sec, which is anti-correlated with the color-temperature. The luminosity sharply reached its peak at $\sim 2 \times 10^{38}$ erg/s and was saturated for roughly 70 sec at the maximum value. It is the typical behavior of an X-ray burst from a neutron star where the luminosity

has reached the Eddington limit. An expansion in the radius correlated with the temperature decrease as well as the constant luminosity at its peak is the clear indication showing that the PRE occurred in the initial 80 sec. Then, during the decay of the burst, $\sim$ 100 sec and later after the onset, the apparent radius again showed a gradual increase. This may be related to the non-Planckian nature of the emission, and does not reflect true change of the photospheric radius of the burst.

The time-resolved burst spectra are well-reproduced by the blackbody model for the majority of the observed period during the burst, but they sometimes show deviations. Especially, large deviations are seen in the spectra in the latter half of the observed cooling phase, as represented by the relatively large χ^2_ν (> 1.5) after $\sim$ 120 sec. It is usually expected that non-Planckian effects become small during the decay of the burst when the temperature becomes low. Thus the energy spectra should be better expressed with an absorbed blackbody than those near the peak of the burst. However, figure 3.3 shows that it is not the case. The reduced chi-square distributions of the time-resolved burst spectra are presented in figure 3.4. Indeed, the reduced chi-square distributions of the burst spectra in the latter part of the burst (136–192 sec) are shifted to the larger value than those in the early part of the burst (0–136 sec), where the reduced chi-squares are concentrated around 1.0 as expected for the acceptable model. This suggests that the burst spectra in the latter part of the burst are distorted from an absorbed blackbody model not by just the statistical fluctuation, but the distortion is intrinsic to the source emission.

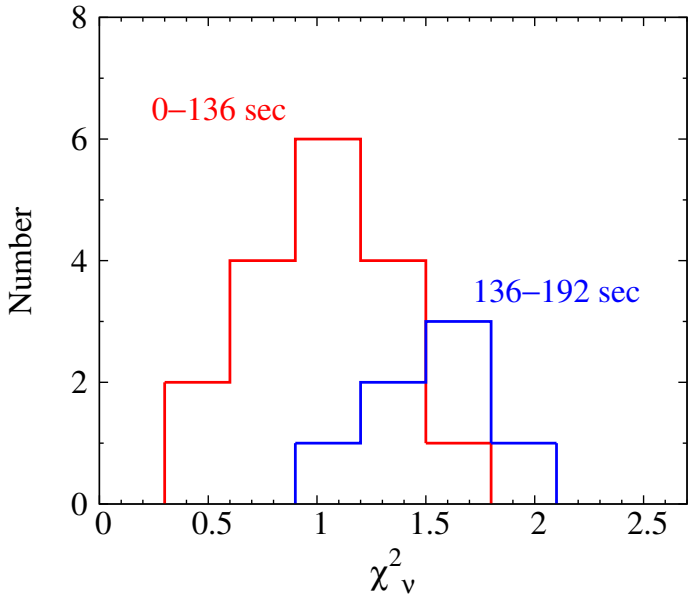

Figure 3.4: Reduced chi-square distributions of the time-resolved burst spectra for 0–136 sec (red) and for 136–192 sec (blue) are plotted, respectively, as histograms. The reduced chi-squares are obtained from the burst spectra of each energy bin by fitting an absorbed blackbody model.

3.3 Spectral Analysis in the Latter Half of the Observed Cooling Phase

We performed detailed analysis of the burst spectrum during the cooling phase to find out the origin of the poorly matched model, represented by the relatively large reduced chi-square. To improve statistics, we also used the BI-CCD data in addition to the FI-CCD data, as the telemetry saturation did not occur in the decay of the burst. Furthermore, we summed up all the data in each CCD during the time-region B in figure 3.3, where χ^2_ν is large and where the variation of the burst parameters is negligibly small. Figure 3.5 shows the obtained burst spectra in the time-region B. The FI-CCD and BI-CCD spectra were simultaneously fitted with the absorbed blackbody model. We included a constant component in the model to absorb the calibration uncertainty in the effective area between the FI- and BI-CCDs. The best-fit models and residuals are overlaid in figure 3.5. The fit is found to be poor with $\chi^2_\nu \sim 2.2$, leaving a broad feature in the residuals above 7 keV and a soft excess below 2 keV. How can we address the issue? Over-estimation of the column density in the spectral fitting often produces positive residuals below 2 keV (the soft excess). Only the spectral feature in the current model that can reproduce both the roll-off feature in the residuals above 7 keV and the soft excess is the iron edge in the phabs component. In that sense, it is likely the soft excess is related to the roll-off above 7 keV, where the current model is too simple to explain them well. Thus, if the appropriate model-component to explain the roll-off is added, the residual below 2 keV may well disappear.

Based on this consideration, the following six models are examined to reproduce the broad feature above 7 keV, all of which are possible models in burst sources: (i) absorption edge ("simple edge" model), (ii) a relativistically-broadened emission line ("diskline" model), (iii) reflection by cold matter ("reflection" model), (iv) partial-covering absorption ("pcfabs" model), (v) a smeared absorption edge due to the NS spin (Doppler-smeared absorption edge model, hereafter "dpsmedge" model), and (vi) two-temperature blackbody ("2bbody" model).

Firstly, the simple edge model is examined. In this model, a photo-electric absorption edge model (edge) is multiplied to the absorbed blackbody model. The unfolded energy spectra and the best-fit models are plotted in the upper panel of figure 3.6, and the ratios of the best-fit models, which are convoluted with the response functions of the detector, to the observed spectra in the lower panel. Note that the unfolded spectrum is calculated from the observed one simply divided by the energy-dependent detection efficiencies defined as the ratio of the folded model and the unfolded model. Thus, precisely speaking, the unfolded spectrum depends on the assumed spectral model. The best-fit parameters are listed in table 3.1 The fit is not acceptable with $\chi^2_\nu = 1.49$, whose probability is calculated to be $\sim 0.1\%$ for about 100 degrees of freedom, and the significant residuals remain above ~ 7 keV. The residual implies that the observed spectral feature is rather dull and a sharp model, such as the absorption edge model, cannot reproduce the feature.

Secondly, the relativistically-broadened emission line, so-called disk line model (diskline: Fabian et al. 1989) is examined. We tried two cases for the disk inclina-

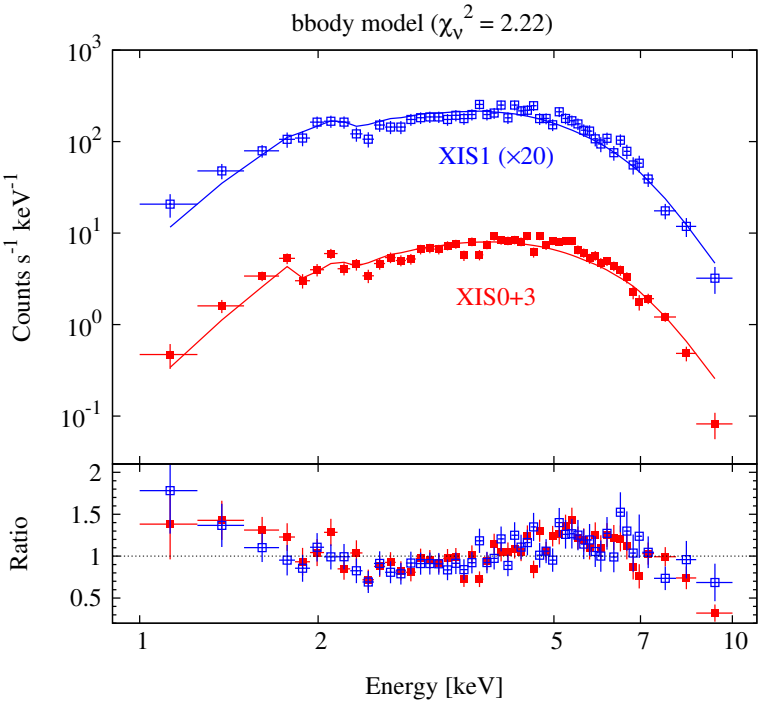

Figure 3.5: Energy spectra of the burst in the latter half of the observed cooling phase (144–192 sec in figure 3.3) are plotted in the upper panel. The filled squares (red) are for the XIS 0 and 3 (FI-CCD) data and the open squares (blue) are for the XIS 1 (BI-CCD) data. The solid lines indicate the best-fit models of an absorbed blackbody. The data and model associated with the XIS 1 are multiplied, respectively, by twenty in order to be easily viewed. The fit residuals are shown in the lower panel as ratio of the observed spectra to the best-fit models. The horizontal bars of the data points represent integration energy ranges, and the vertical bars errors in the 68% (1σ) confidence limit. A relatively large residual structure is seen above 5 keV.

Table 3.1: Best-fit parameters of the edge model.

Component	Parameter	Value
	constant × phabs × bbody × edge	
	χ^2_ν/d.o.f. = 1.49/96	
constant	Relative normalization factor	0.89 ± 0.03
phabs	$N_{\rm H}$ [10^{22} cm^{-2}]	1.75 ± 0.11
bbody	$kT_{\rm c}$ [keV]	1.54 ± 0.04
	Bolometric luminosity [10^{38} erg s^{-1}]	0.58 ± 0.01
edge	$E_{\rm edge}$ [keV]	7.71 ± 0.06
	Optical depth ($\tau_{\rm edge}$)	1.55 ± 0.23

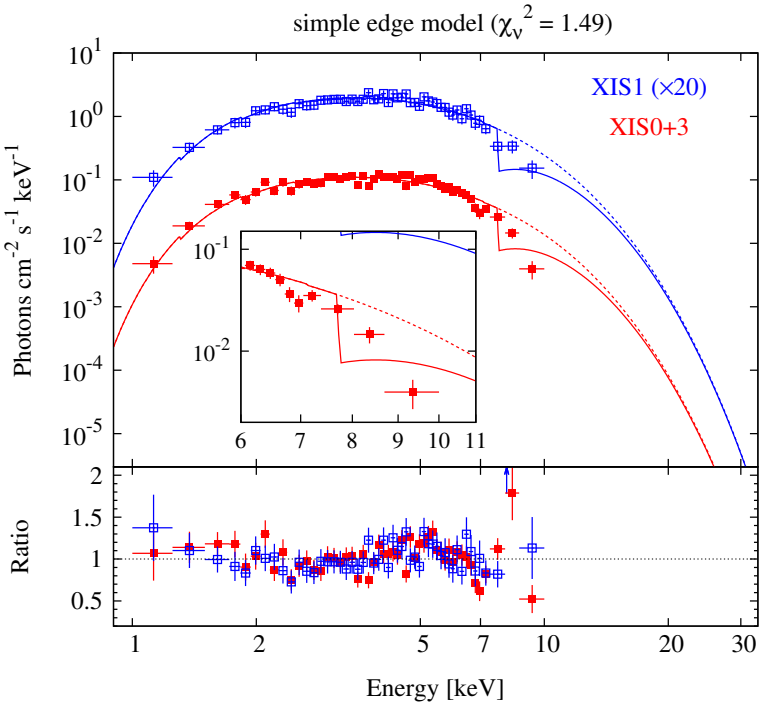

Figure 3.6: Unfolded energy spectra of the burst in the latter half of the observed cooling phase (144–192 sec in figure 3.3) are plotted in the upper panel. The filled squares (red) are for the XIS 0 and 3 (FI-CCD) data and the open squares (blue) are for the XIS 1 (BI-CCD) data. The best-fit models of an absorbed blackbody multiplied by an absorption edge and those without the absorption edge component are also plotted as solid and dashed lines, respectively. The data and model associated with the XIS 1 are multiplied, respectively, by twenty in order to be easily viewed. The close-up spectra of XIS 0 and 3, in which the spectral feature is seen, are shown in the inset. The fit residuals are shown in the lower panel as ratio of the observed spectra to the best-fit model. The horizontal bars of the data points represent integration energy ranges, and the vertical bars errors in the 68% (1σ) confidence limit.

tion. In one case, appropriate for GRS 1747−312 (in't Zand et al. 2003a), it is fixed to 74.5°. In the other case, corresponding to the case that the burst is produced by the contamination source, the disk inclination is optimized in the model fitting. In this case, no information is available for the disk inclination. However, the burst emission is clearly seen with little obscuration by e.g., outer accretion disk, thus large inclination close to 90° is clearly excluded. Because the outer accretion disk typically subtend 40–60°, inclination angle is considered to be larger than 70–80°. It is noted that the disk inclination is required in two of the following models (the reflection model and dpsmedge). So, we adopted the same method also for the spectral analysis with dpsmedge model. The line emissivity is parameterized as a power-law function with radius and is assumed to follow the inverse-square law. To produce the broadest spectral feature with the diskline model, the inner radius, $r_{\rm in}$, of the disk is fixed to the minimum value, $6R_{\rm s}$, where $R_{\rm s}$ is the Schwarzschild radius. The best-fit parameters and the ratios of the fitting residuals are given in table 3.2 and the middle panel of figure 3.7, respectively. The χ^2_ν is still large, 1.47, and so are the residuals at > 6 keV. When the disk inclination is set free, it tends to become larger converging to the case of 74.5°. If we force to set a smaller inclination angle, say 30°, the profile of the disk line become sharper and the χ^2_ν become large with $\chi^2_\nu \sim 1.8$.

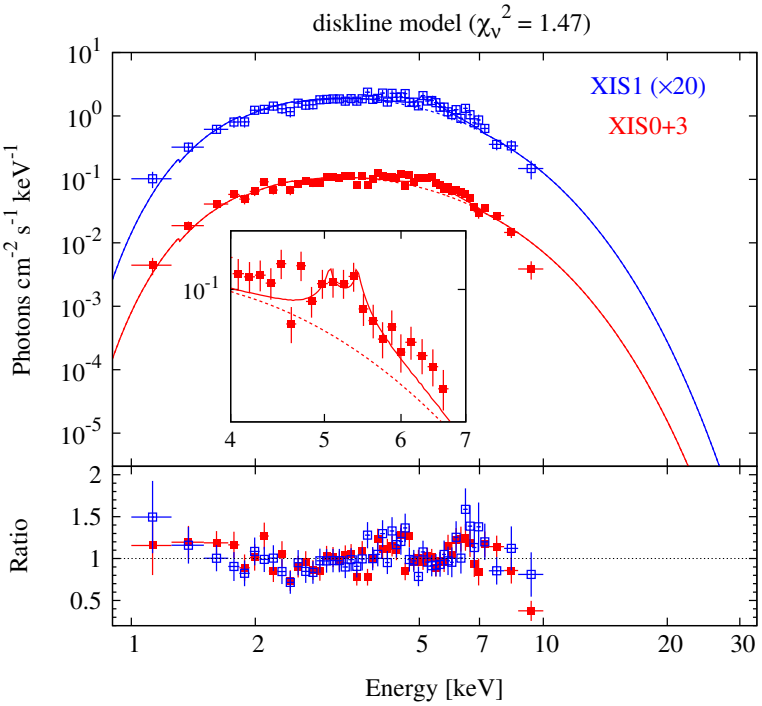

Figure 3.7: Same as figure 3.6, but the model is diskline added to the absorbed blackbody for the upper and lower panels, respectively.

Thirdly, the model of reflection by cold matter is applied. In this model, the blackbody component was convoluted with the reflection component (reflect: Magdziarz & Zdziarski 1995). The best-fit parameters and the ratios of the fitting

Table 3.2: Best-fit parameters of the diskline model.

Component	Parameter	Value
	constant × phabs × (bbody + diskline)	
	χ^2_ν/d.o.f. = 1.47/96	
constant	Relative normalization factor	0.89 ± 0.03
phabs	$N_{\rm H}$ [10^{22} cm^{-2}]	1.94 ± 0.11
bbody	$kT_{\rm c}$ [keV]	1.33 ± 0.02
	Bolometric luminosity [10^{38} erg s^{-1}]	0.47 ± 0.01
diskline	$E_{\rm line}$ [keV]	5.24 ± 0.05
	Radial dependency of the line emissivity	(r^{-2})
	Intensity [10^{-2} photons cm^{-2} s^{-1}]	4.48 ± 0.51
	$r_{\rm in}$ [$R_{\rm s}$]	(6)
	$r_{\rm out}$ [$R_{\rm s}$]	(1000)
	Disk inclination angle	(74.5°)

residuals are given in table 3.3 and the bottom panel of figure 3.8, respectively. This model gives a good fit with $\chi^2_\nu \sim 1.1$. However, the best-fit reflection scaling-factor (1.0 for an isotropic source above the disk) is extremely large, 104 ± 30. Such a large scaling-factor would require that the direct beam from the X-ray emitting source be almost completely blocked and that only the reflection component be visible. However, such a geometry is contradictory to the observational fact that the bolometric luminosities during the burst reached the Eddington limit. Although this result is obtained for the inclination of 74.5°, we confirmed that it is essentially independent of the assumed inclination. Therefore, this model is not plausible.

Fourthly, the partial-covering absorption model (pcfabs) is examined. The pcfabs model is multiplied to the absorbed blackbody model. The best-fit parameters and the ratios of the fitting residuals are given in table 3.4 and the top panel of figure 3.9, respectively. The pcfabs model gives a good fit with $\chi^2_\nu \sim 1.0$. The best-fit column depth and covering fraction of the pcfabs parameters are $22.6 \pm 2.5 \times 10^{22}$ cm^{-2} and 0.78 ± 0.03, respectively.

Fifthly, the dpsmedge model is applied. In this model, an absorption edge is assumed to be formed in the neutron star atmosphere during the burst and to be smeared by the spin of the neutron star. Because such a model is not available in XSPEC, a simple program is developed to calculate the Doppler-smeared absorption edge, which is imported for XSPEC as the table model. Details of the model is described in the Appendix A. The Doppler-smeared absorption edge model (dpsmedge) is multiplied to the absorbed blackbody model. The best-fit parameters and the ratios of the fitting residuals are given in table 3.5 and the middle panel of figure 4.3, respectively. The dpsmedge model gives a good fit

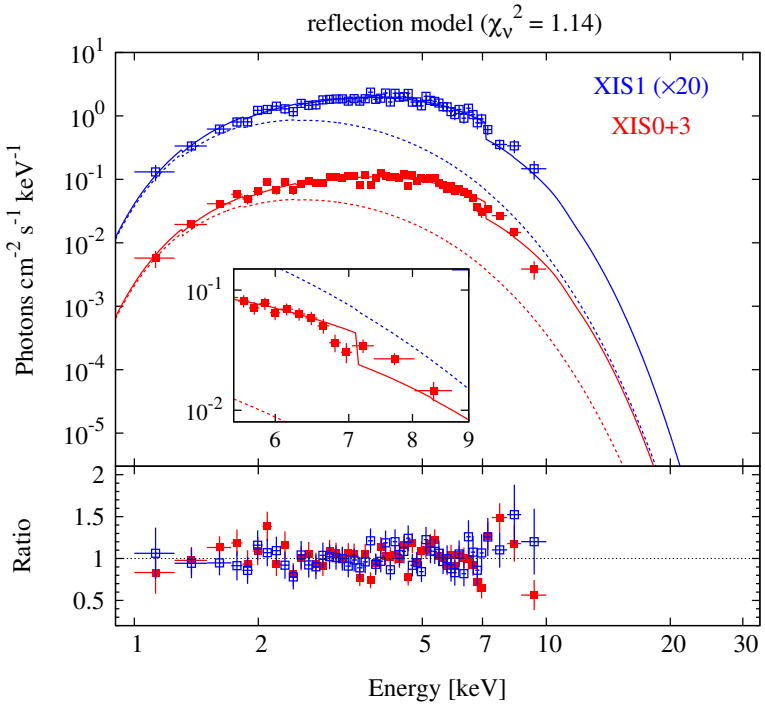

Figure 3.8: Same as figure 3.6, but the model is reflection multiplied to the absorbed blackbody for the upper and lower panels, respectively.

Table 3.3: Best-fit parameters of the reflection model.

Component	Parameter	Value
	constant × phabs × reflect × bbody	
	χ^2_ν/d.o.f. = 1.14/97	
constant	Relative normalization factor	0.90 ± 0.03
phabs	$N_{\rm H}$ [10^{22} cm^{-2}]	1.38 ± 0.16
bbody	$kT_{\rm c}$ [keV]	0.95 ± 0.02
	Bolometric luminosity [10^{38} erg s^{-1}]	1.27 ± 0.03
reflection	Reflection scaling-factor	104 ± 30
	Disk inclination angle	(74.5°)

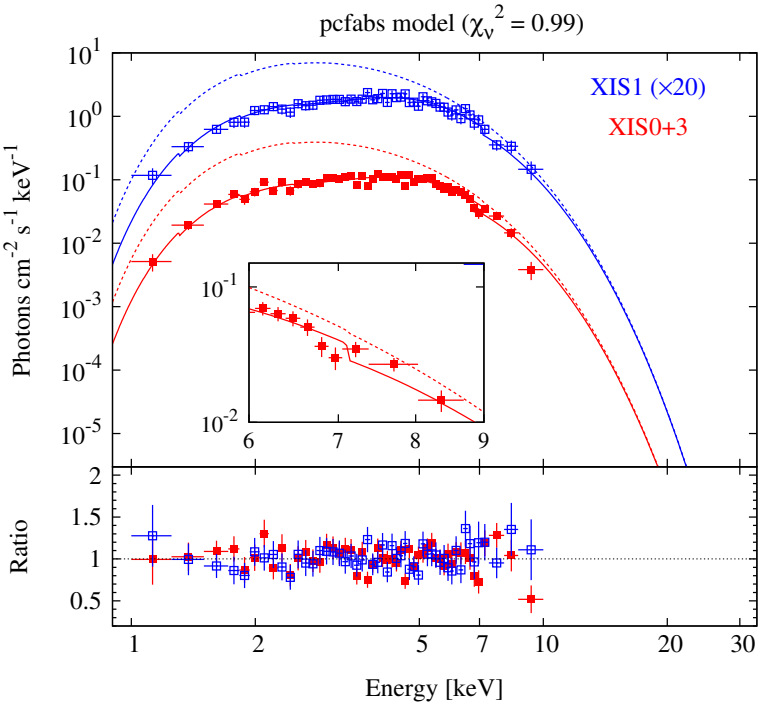

Figure 3.9: Same as figure 3.6, but the model is pcfabs multiplied to the absorbed blackbody for the upper and lower panels, respectively.

Table 3.4: Best-fit parameters of the pcfabs model.

Component	Parameter	Value
constant × phabs × (pcfabs × bbody) χ^2_ν/d.o.f. = 0.99/96		
constant	Relative normalization factor	0.89 ± 0.02
phabs	$N_{\rm H}$ [10^{22} cm^{-2}]	1.81 ± 0.14
pcfabs	$N_{\rm H}$ [10^{22} cm^{-2}]	22.6 ± 2.5
	Covering fraction	0.78 ± 0.03
bbody	$kT_{\rm c}$ [keV]	1.02 ± 0.03
	Bolometric luminosity [10^{38} erg s^{-1}]	1.24 ± 0.15

with $\chi^2_\nu \sim 0.9$. The best-fit edge energy and spin frequency are 7.15 ± 0.21 keV and $1.76 \pm 0.23(R_{\rm ns}/10$ km) kHz, respectively. We note that the estimated spin frequency has the negative correlation with the assumed value of the disk inclination. For the optical depth, only the lower limit, 7, was successfully obtained. Implications of these parameters are discussed in section 4.

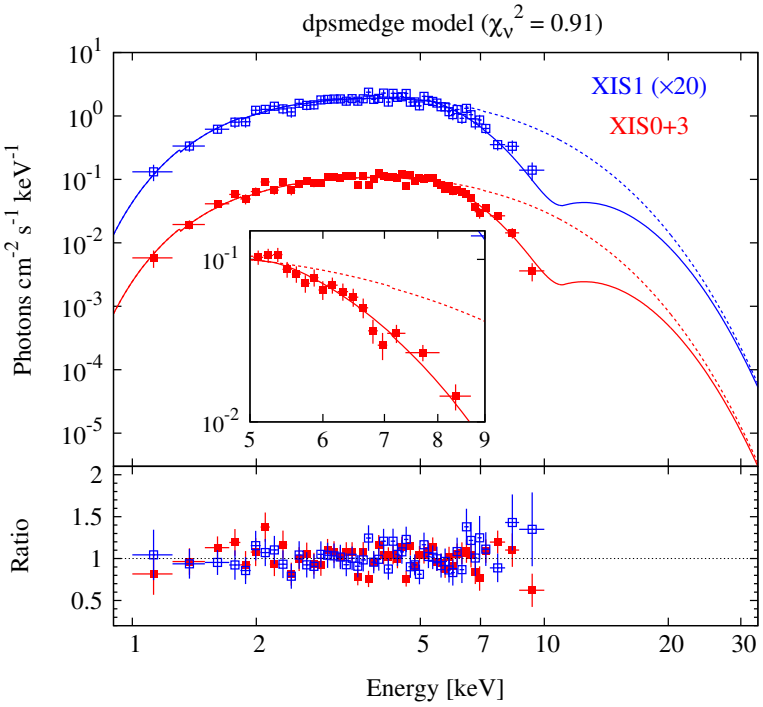

Figure 3.10: Same as figure 3.6, but the model is dpsmedge multiplied to the absorbed blackbody for the upper and lower panels, respectively.

Lastly, the 2bbody model is examined. It is assumed so far that the bursting atmosphere of the neutron star has completely uniform temperature. However, in reality, some temperature variation may be present on the neutron star surface. A two-temperature blackbody is the simplest model to mimic the temperature variation. An additional blackbody is added to the base model of absorbed blackbody. The best-fit parameters and the ratios of the fitting residuals are given in table 3.6 and the bottom panel of figure 3.11, respectively. The χ^2_ν is still large, 1.54, and the positive residual remains below 2 keV due to the larger best-fit column density, 5.5×10^{22} cm^{-2}, than those of previous studies, 1–2 $\times 10^{22}$ cm^{-2} (in't Znad et al. 2000). In addition, the best-fit bolometric luminosities of the bbody component with a lower temperature is comparable with the Eddington luminosity of a NS, in spite of the cooling phase of the burst. Therefore, we conclude that the model is not plausible.

Now that modeling of the average spectrum has been established reasonably, the potential time-variations of the spectral feature is then investigated. For this purpose, the dpsmedge model is adopted, which gives the minimum χ^2_ν for the summed spectra. Energy spectra are calculated in the cooling phase every 16 sec

Table 3.5: Best-fit parameters of the dpsmedge model.

Component	Parameter	Value
	constant × phabs × bbody × dpsmedge χ^2_ν/d.o.f. = 0.91/95	
constant	Relative normalization factor	0.89 ± 0.02
phabs	$N_{\rm H}$ [10^{22} cm^{-2}]	1.31 ± 0.12
bbody	$kT_{\rm c}$ [keV]	1.99 ± 0.13
	Bolometric luminosity [10^{38} erg s^{-1}]	0.84 ± 0.09
dpsmedge	$E_{\rm edge}$ [keV]	7.15 ± 0.21
	Optical depth ($\tau_{\rm edge}$)	> 7
	$\nu_{\rm ns}$ [($R_{\rm ns}$/10 km) kHz]	1.76 ± 0.23
	Disk inclination angle	(74.5°)

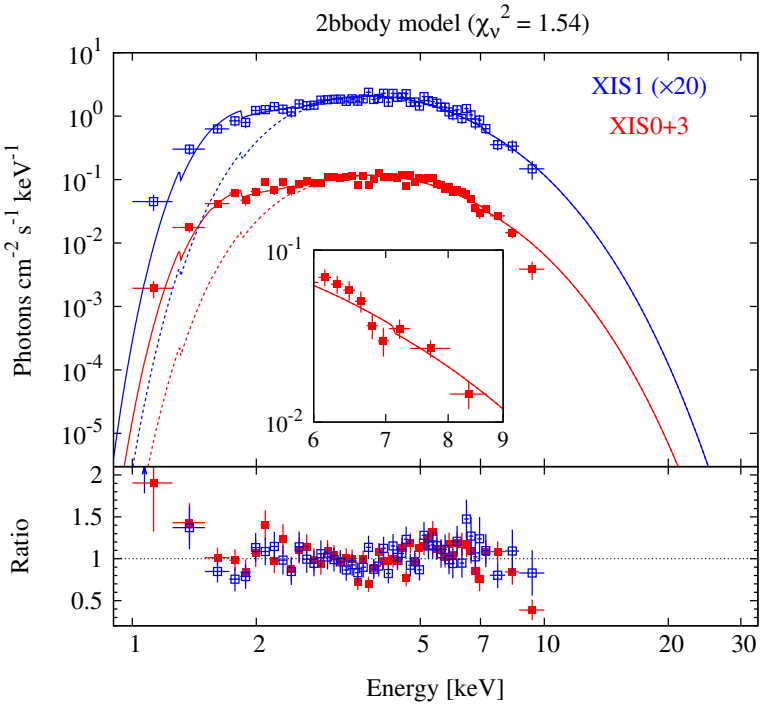

Figure 3.11: Same as figure 3.6, but the model is bbody added to the absorbed blackbody for the upper and lower panels, respectively.

Table 3.6: Best-fit parameters of the 2bbody model.

Component	Parameter	Value
constant × phabs × (bbody1 + bbody2) χ^2_ν/d.o.f. = 1.54/96		
constant	Relative normalization factor	0.90 ± 0.03
phabs	$N_{\rm H}$ [10^{22} cm^{-2}]	5.48 ± 0.43
bbody1	$kT_{\rm c}$ [keV]	0.19 ± 0.01
	Bolometric luminosity [10^{38} erg s^{-1}]	6.44 ± 3.59
bbody2	$kT_{\rm c}$ [keV]	1.20 ± 0.02
	Bolometric luminosity [10^{38} erg s^{-1}]	0.67 ± 0.02

in 1–10 keV. The edge energy and spin frequency are fixed to the best-fit values for the summed spectra (7.15 keV and 1.76 kHz, respectively; table 3.5), because not all the parameters could be simultaneously optimized due to poor statistics of the data. Figure 3.12 shows the time-variations of the optical depths. The optical depth has a tendency to increase gradually with time. This tendency suggests that the spectral feature becomes more prominent later in the cooling phase of the burst.

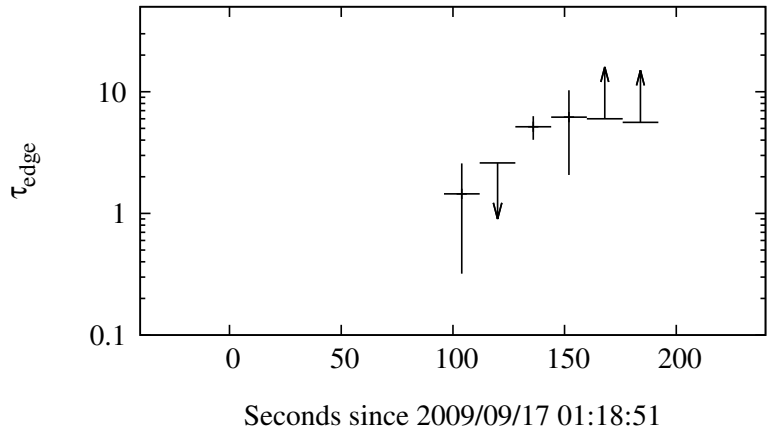

Figure 3.12: Time-variations of the optical depths in the observed cooling phase of the burst. The up and down arrows indicate the minimum and maximum values, respectively. The horizontal bars of the data points represent integration time (16 sec) of the data, and the vertical bars errors in the 90% confidence limit.

Chapter 4

Discussion

An X-ray burst from GRS 1747−312 was detected with Suzaku. The burst was relatively long, and showed moderate PRE. Because the source is known to show PRE bursts, which sometimes have a long duration of a few hundreds seconds, the burst detected here may be a typical one for GRS 1747−312. However, for the first time, the burst showed a distinctive feature in the energy spectra, i.e. a roll-off of the spectrum above ~ 7 keV, in the cooling phase of the burst. Various models have been examined, and it is found that the feature can be reproduced with either the partial-covering model or the Doppler-smeared absorption edge model (section 3). In this section, I first discuss the spectral feature during the burst in the context of non-Planckian nature, then the two candidate spectral models.

4.1 Non-Planckian Nature of the Burst Spectra

Energy spectra during X-ray bursts are generally well represented by a blackbody modified with the low-energy absorption. However, deviation from a blackbody due to the electron scattering in the hot atmosphere of neutron stars has been also commonly observed (see, e.g., van Paradijs et al. 1989). When electron scattering becomes significant, the emissivity of the source photons is reduced, resulting in the different color- and effective temperatures. Although simple difference between the color- and effective temperatures does not distort the spectral shape, detailed model calculations show deviations from the blackbody spectrum, which depend on various parameters such as luminosity and abundance (Ebisuzaki 1987; Madej et al. 2004; Majczyna et al. 2005; Suleimanov et al. 2012). Recently, Inoue (2015) gave a simple analytical formula to approximate the energy spectra from the bursting atmosphere, which is dominated by the Compton scattering: a blackbody modified by the filter function defined as:

$$f(E, kT) = \max\left(1 - \frac{E}{3kT} \times \left(1 - \exp\left(-\frac{E}{kT}\right)\right), 0\right), \tag{4.1}$$

where E is the photon energy and kT is the temperature of the atmosphere. This filter function tends to reduce high energy photons, which practically creates the spectral roll-off. Figure 4.1 shows the fit result of the burst spectra in the latter

half of the observed cooling phase (figure 3.5) with a blackbody modified with this filter function. The temperature of the filter function is fixed to that of the blackbody model. The best-fit parameters are listed in table 4.1. The fit gives a $\chi^2_\nu \sim 1.1$. Thus, the model reproduces the observed spectra well.

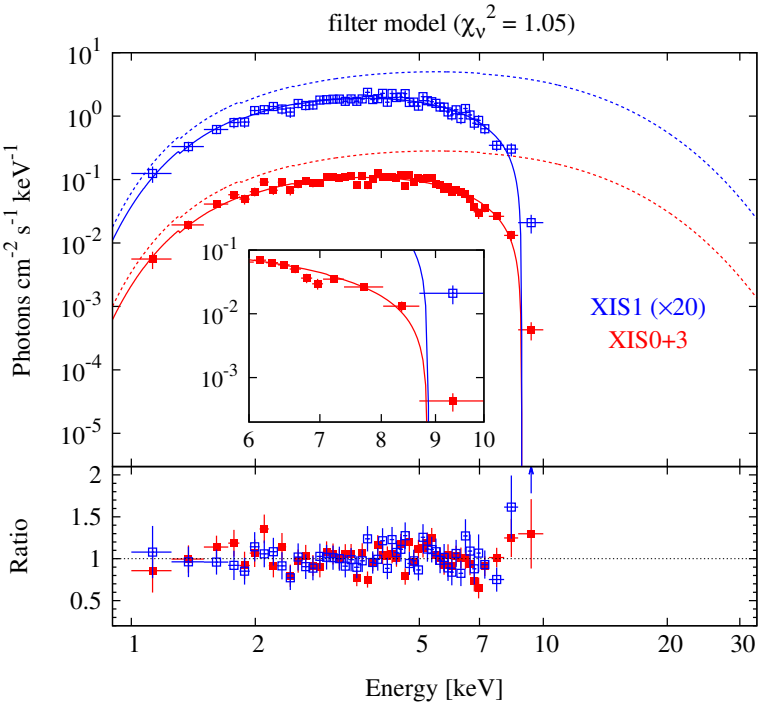

Figure 4.1: Same as figure 3.6, but the model is an absorbed blackbody modified with the filter function (Inoue 2015). See text for the filter function.

The roll-off of the spectra was observed only in the latter half of the cooling phase of the burst. As shown in figure 3.12, the roll-off was moderate at first and became more significant later. This time-variation may be understood in the context of the Compton scattering, as follows. As represented with the filter function, roll-off starts at higher energy when the temperature of the burst atmosphere is high. If the temperature of the atmosphere is sufficiently high in the early part of the burst (except the PRE phase), the roll-off of the spectrum shifts beyond the Suzaku/XIS energy band. When the atmosphere cools down, the roll-off shifts to lower energy and becomes significant in the observed energy spectra. The time-variation of the edge depth in figure 3.12 was derived with the edge energy being fixed. In fact, the data are found to be also consistent with the change of the edge energy instead, and hence with the above-mentioned interpretation with Compton scattering. One cannot determine which interpretation is more appropriate due to the limited statistics. This model will be further investigated in subsection 4.4.

In the context of the non-Planckian spectra, detections of some atomic features have been reported in the burst spectra of neutron stars. Examples include the detection of absorption edges in the superexpansion bursts from 4U 0614+091 and 4U 1722−30 (in't Zand et al. 2010). The edges were detected during the expansion

Table 4.1: Best-fit parameters of filter model

Component	Parameter	Value
	constant × phabs × bbody × filter χ^2_ν/d.o.f. = 1.05/98	
constant	Relative normalization factor	0.89 ± 0.02
phabs	$N_{\rm H}$ [10^{22} cm^{-2}]	1.38 ± 0.08
bbody	$kT_{\rm c}$ [keV]	3.13 ± 0.03
	Bolometric luminosity [10^{38} erg s^{-1}]	5.01 ± 0.10
filter	kT [keV]	3.13±0.03

phase and showed a simple profile, i.e. no smearing was detected within the energy resolution of the Proportional Counter Array (PCA: Jahoda et al. 2006) onboard RXTE. These features may originate from H-like or He-like ions of iron peak elements in the burst ashes exposed to the expanded photosphere (in't Zand et al. 2010). Combination of a broad emission line and an absorption edge was observed in the superburst from 4U 1820−30 with RXTE PCA (Strohmayer & Brown 2002). They argued that the feature was likely to be produced by the reflection of the burst flux from the inner accretion disk. The edge features detected so far during the X-ray bursts from neutron stars have been observed either in the expansion phase or throughout the burst. In the Suzaku observation of GRS 1747−312, the spectral feature was detected only in the decay phase. Furthermore, the edge features detected here were clearly smeared, whereas those reported in the literature were all narrow, although we should note that the energy resolutions of the detectors are also different. It is likely that the spectral feature detected in the Suzaku data have a different origin from those detected in the past observations.

4.2 Partial-Covering Absorption

Partial covering is observed in dip sources regularly. Given that a dip-like decrease of the flux was detected in the Suzaku data of GRS 1747−312 (Saji et al. 2015), it is not surprising that the partial-covering model worked well to reproduce the burst spectra of this source (section 3.3, table 3.4). In this subsection, we discuss whether the partial-covering model is scientifically appropriate or not for this source.

If the partial covering is responsible for the spectral feature during the burst, the covering material should be absent in the early part of the burst and should suddenly appear later during the cooling phase. Covering material is usually thought to be located near the outer edge of the accretion disk, where the disk is the thickest. In that case, its presence would be hardly affected by an X-ray burst. On the other hand, its ionization degree may change as it is illuminated with intense X-rays from the burst, which may make the partial-covering scenario viable. In fact, enhanced soft X-ray flux during bursts due to the photo-ionization of the absorb-

ing material was observed from EXO 0748−676 (Asai & Dotani 2006). According to this scenario, partial-covering material can be almost completely photo-ionized in the early part of the burst and accordingly does not work as absorber. Then, its ionization degree will decrease in the cooling phase due to the reduction of X-ray flux, and the material will start working as absorber.

In order to verify this scenario, the partial-covering model with ionized absorber is examined, using partcov and absori (Done et al. 1992) models available in XSPEC (hereafter pcfabsi model). In this model, the ionizing flux is assumed to have, rather arbitrary, a power-low spectrum with a photon index of 2, because the results is almost insensitive to the spectral shape. Also, to deal with the problem of parameter-coupling between the column density and the ionization degree, the column depth is fixed to 10.5×10^{22} cm^{-2}, which is the best-fit value derived from the persistent flux before and after the burst (Saji et al. 2015). The best-fit parameters are listed in table 4.2, and the ratios of the best-fit model to the spectra are plotted in the upper panel of figure 4.2. The model is found to give a poor fit with $\chi^2_\nu \sim 1.3$. Furthermore, the ionization parameter is consistent with zero (< 0.3 in the 90% confidence limit). This means that the absorber should be almost or completely neutral. Indeed, it is expected from the observed spectrum (figure 3.5) because the roll-off above 7 keV suggests the (partial-covering) absorber to be neutral.

Above fitting result leaves only the possibility that the absorber is completely photo-ionized in the burst peak and becomes neutral in the burst decay. We introduce the ionization parameter, $\xi = L/nr^2$, of the material, where L is the X-ray luminosity, n the density of the material, and r the distance of the material from the X-ray source. If we take Fe as an example, it is almost neutral when ξ is small, say < 10, He-like ion becomes dominant when $\xi \sim 10^3$, and it is almost completely ionized when $\xi \sim 10^4$. The burst luminosity decreased by a factor of 3 from the peak to the decay where the roll-off become significant in the energy spectra. Because the density (n) and location (r) of the absorber cannot change largely during the burst, reduction of ξ parameter from the burst peak to the decay may be at most a factor of 3. This amount of change in ξ is insufficient to cause large change in the ionization degree of the absorber. Thus it is difficult to explain that emergence of the spectral roll-off only in the decay of the burst by the variation of the photo-ionization degree of the partial covering absorber.

4.3 Doppler-Smeared Absorption Edge

An absorption edge may appear in the burst spectra when the burst flux from the bottom of the neutron star atmosphere, where the bursts ignite, passes through the relatively cold layers. Furthermore, if the absorption edge of this kind is present in the spectrum, the edge feature should be smeared due to rapid spin of neutron stars. As seen in section 3, the Doppler-smeared absorption edge model gives an acceptable fit. However, the best-fit parameters are implausible; the spin frequency, $1.76 \pm 0.23 (R_{\rm ns}/10\ {\rm km})$ kHz, is too large and the optical depth, $\tau_{\rm edge} > 7$, is also large. For example, the spin frequencies of X-ray bursters measured from

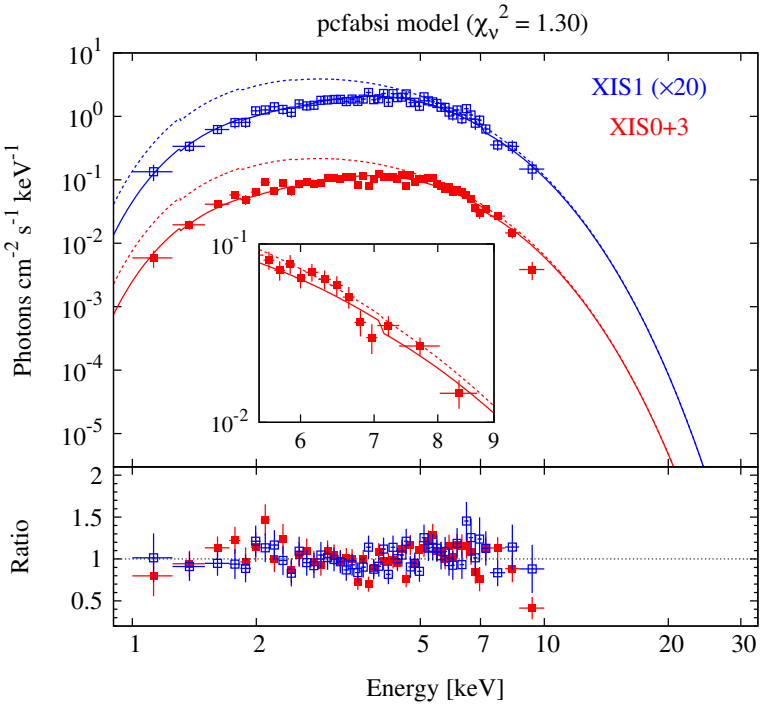

Figure 4.2: Same as figure 3.6, but the models is pcfabsi multiplied to the absorbed blackbody for the upper and lower panels, respectively.

Table 4.2: Best-fit parameters of pcfabsi model.

Component	Parameter	Value
constant × phabs × (partcov × absori) × bbody χ^2_ν/d.o.f. = 1.30/96		
constant	Relative normalization factor	0.90 ± 0.03
phabs	$N_{\rm H}$ [10^{22} cm^{-2}]	1.37 ± 0.15
partcov	Covering fraction	0.67 ± 0.04
absori	Photon index	(2.00)
	$N_{\rm H}$ [10^{22} cm^{-2}]	(10.5)
	Temperature of absorber [K]	(3×10^4)
	Ionization parameter	< 0.30
	Redshift	(0.00)
	Abundance of Fe element	(1.00)
bbody	$kT_{\rm c}$ [keV]	1.16 ± 0.02
	Bolometric luminosity [10^{38} erg s^{-1}]	0.74 ± 0.03

the burst oscillations all range between 270–620 Hz (Strohmayer 2001). Indeed, the spin frequency of 1.76 kHz is comparable with the break-up frequency of a neutron star. The roll-off of the observed energy spectrum is so dull that it may require large smearing if fitted with a single edge. On the other hand, in reality, two or more ions and/or species may be involved in the spectral feature, whereas the model used here in the spectral fitting (section 3.3, table 3.5) took only one element into account. If multiple ions are involved, the spectrum may well be explained without requiring large smearing.

To test this hypothesis, another Doppler-smeared absorption edge component is added to the model of dpsmedge (hereafter referred to as 2dpsmedge model) and the spectrum is fitted with such a model. In the fitting, the spin frequency is fixed at several different values, ranging 0.3–1.2 kHz, because not all the parameters could be simultaneously optimized due to poor statistics of the data. As an example, the best-fit parameters for 0.6 kHz are listed in table 4.3, and the ratios of the best-fit model to the spectra are plotted in the lower panel of figure 4.2. The model gives a good fit with $\chi^2_\nu = 0.94$. The best-fit edge energies are found to be 6.31 ± 0.12 and 8.13 ± 0.16 keV with the optical depths of 0.87 ± 0.11 and 2.92 ± 0.43, respectively. The χ^2_ν and best-fit edge parameters in principle depend on the assumed spin frequency. Figure 4.4 plots the resultant variation of χ^2_ν and the edge parameters against the assumed spin frequencies. The fit is similarly good regardless of the assumed spin frequency. The χ^2_ν take a minimum at the spin frequency of ~ 0.9 kHz and the allowable spin frequency range in the 90% confidence limit was such that the lower limit was ~ 0.6 kHz but the upper limit could not be constrained. However, the spin frequencies should be lower than the break-up frequency of a neutron star, which is typically ~ 1.2 kHz (see equation 1.1). Based on this consideration, we conclude that the most plausible range of the spin frequency is 0.6–1.2 kHz, where the best-fit edge parameters vary as follows: lower edge energy ranging between 6.23–6.44 keV with $\tau_{\rm edge} = 0.87$–1.12 and higher edge energy, between 8.01–8.26 keV with $\tau_{\rm edge} = 3$–> 3. Although the fit by the model of 3dpsmedge, which is added one more Doppler-smeared adsorption edge component, is also acceptable with $\chi^2_\nu = 0.88$, reduction of chi-squared is small and 3dpsmedge is not preferred statistically over the 2dpsmedge. In addition, in the case of 3dpsmedge, the errors of edge parameters cannot be estimated due to strong coupling among the edge parameters. In reality, the spectral feature detected here may include large number of small absorption edges, which correspond to various elements and their ionization degrees. The two absorption edges obtained by fitting may be the two most prominent ones among many possible absorption edges.

We now discuss which elements/ions are most likely to be responsible for the observed edges. For this purpose, we utilize the difference between the two edge energies, as it is difficult to guess the burst products directly. From the abovementioned best-fit parameters, the energy difference of these two edges is estimated to be ~ 1.9 keV, corresponding to $29 \pm 5\%$ if we adopt the lower energy as a reference. The fractional difference of the two edge energies does not change very much, even if the possible range of spin frequency is taken into account, because the two edge energies show positive correlation (figure 4.5). It is difficult to explain

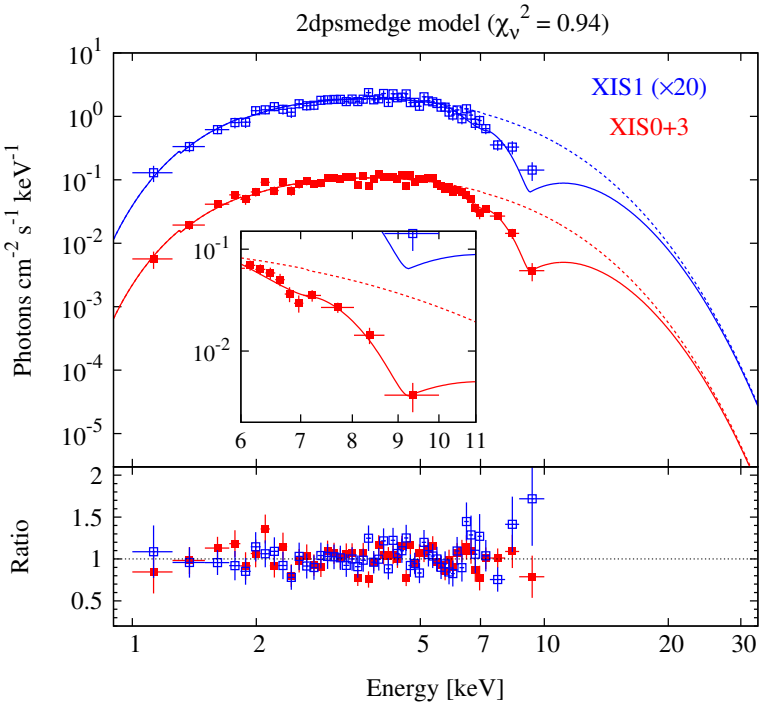

Figure 4.3: Same as figure 3.6, but the model is 2dpsmedge multiplied to the absorbed blackbody for the upper and lower panels, respectively.

Table 4.3: Best-fit parameters of 2dpsmedge model.

Component	Parameter	Value
constant × phabs × bbody × dpsmedge1 × dpsmedge2		
χ^2_ν/d.o.f. = 0.94/94		
constant	Relative normalization factor	0.88 ± 0.02
phabs	$N_{\rm H}$ [10^{22} cm^{-2}]	1.37 ± 0.11
bbody	$kT_{\rm c}$ [keV]	1.90 ± 0.09
	Bolometric luminosity [10^{38} erg s^{-1}]	0.77 ± 0.06
dpsmedge1	$E_{\rm edge}$ [keV]	6.31 ± 0.12
	Optical depth ($\tau_{\rm edge}$)	0.87 ± 0.11
	$\nu_{\rm ns}$ [kHz]	(0.60)
	Inclination angle	(74.5°)
dpsmedge2	$E_{\rm edge}$ [keV]	8.13 ± 0.16
	Optical depth ($\tau_{\rm edge}$)	2.92 ± 0.43
	$\nu_{\rm ns}$ [kHz]	(0.60)
	Disk inclination angle	(74.5°)

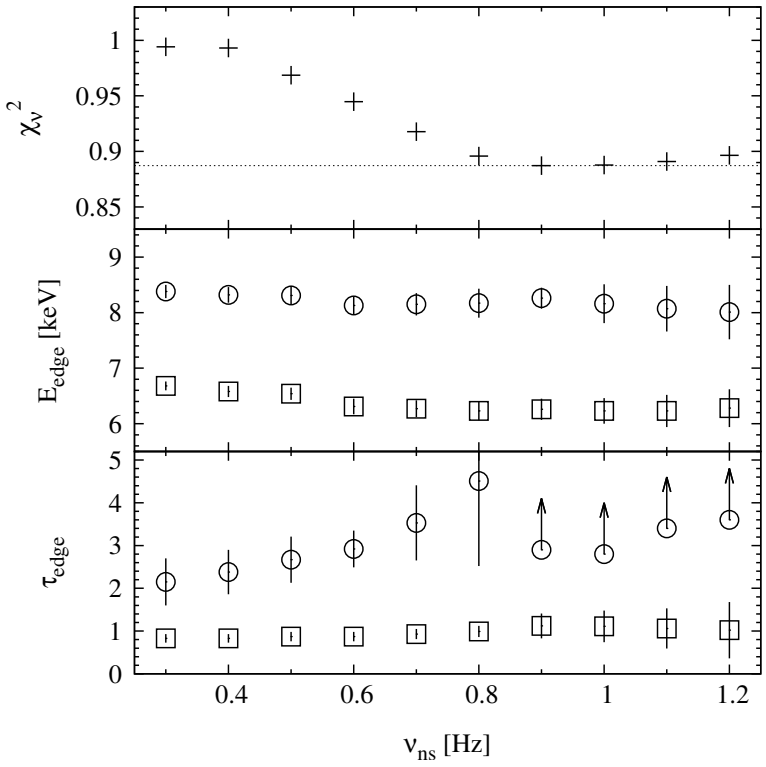

Figure 4.4: Variations of the major parameters (a reduced chi-square, an edge energy, and an optical depth from top to bottom) obtained against the spin frequency by fitting with the 2dpsmedge model. In the middle and bottom panels, the vertical bars errors in the 90% confidence limit.

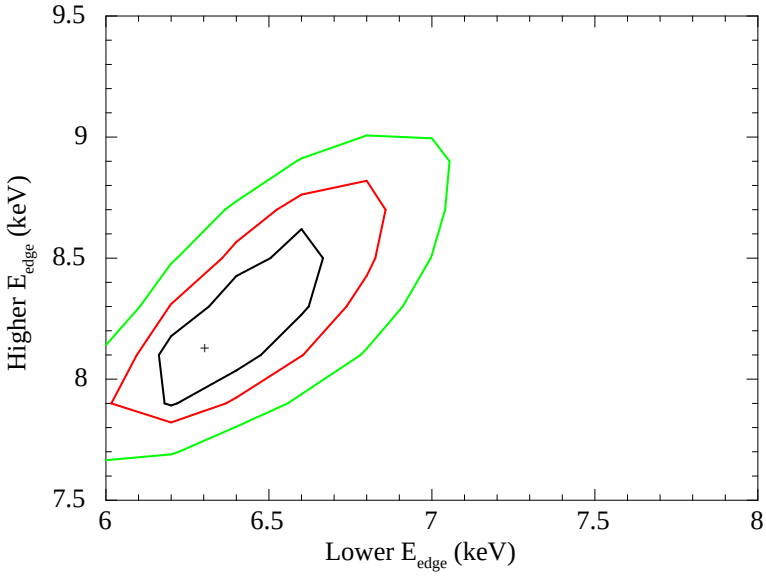

Figure 4.5: Correlation of the two edge energies is shown. 68% (black), 95% (red), and 99% (green) confidence contours of the lower and higher edge energies obtained from the fitting by the 2dpsmedge model with 600 Hz.

the energy difference of these two edges, $\sim 29\%$, by a single element with different ionization degrees. In what follows, we consider the relative difference in the edge energies, taking into account the fact that they may be gravitationally red-shifted. If we adopt He-like and H-like iron ions, for example, their edge energies in the laboratory system are 8.83 and 9.28 keV, respectively. Their difference is only 5%. If (nearly) neutral iron was involved to form the edge, the separation of the edge energies would be as large as $\sim 30\%$. On the other hand, it is highly unlikely that abundant lowly-ionized iron exists in the burst atmosphere, given the observed burst temperature of a few keV. This situation does not change very much even if other elements of major burst products are considered. It is also confirmed that any other single element with different ionization states alone would not explain well the observed two edges.

We then consider pairs of elements as the sources for the two edges. Edge energies of H-like ions with the atomic number Z are approximated as $E_{\rm edge} = 13.6Z^2$ eV (see, e.g., Bildsten et al. 2003). The relative difference of the edge energies for the two neighboring elements (Z and $Z+1$) is then calculated to be $\delta E_{\rm edge}/E_{\rm edge} = (2Z+1)/Z^2$. The relative difference of 29% in GRS 1747−312 corresponds to $Z \sim 7$. This atomic number is clearly inconsistent with the observed edge energies. Similarly, for the given two elements of Z and one of Z+2, Z+3, and $Z+4$, the atomic numbers are calculated to be $Z \sim 15$, 22, and 29, respectively. The observed edge energies indicate that the combination of Z and $Z+4$ is most plausible. Among the elements near $Z \sim 29$, it is conjectured that Zn and Se are the plausible combination for the difference in the atomic number of 4, taking account of the composition of burst ashes (Woosley et al. 2004). Other possible combinations are Fe and Zn or Ni and Ge, based on Weinberg et al. (2006). If real, the production of such heavy elements should result in a long duration of the burst, as mentioned in section 1.2.4.1. Indeed, as seen in the figure 3.2, the light curve of the burst shows a long duration. However, the last combination may not be plausible because for example, ^{62}Ge and ^{64}Ge decay to ^{62}Zn in less than 1 sec and ^{64}Zn in ~ 1 min, respectively, and will be absent late in the cooling phase.

If the above-mentioned elements of Fe, Zn, and Se are involved to form the absorption edges, they should be the products of nuclear burning in the burst. In fact, some ashes of PRE bursts may be exposed at the neutron star surface. Weinberg, Bildsten & Schatz (2006) showed that the maximum vertical extent of the convective region during the PRE bursts can be sufficiently large that some ashes of burning are ejected by the radiation-driven wind during the PRE phase and are exposed on the neutron star surface after the PRE phase. Composition of the burst ashes can be estimated via model calculations of bursts, which include extensive nuclear-reaction network. Woosley et al. (2004) developed the multi-zone models of bursts and showed that nuclear reaction in the bursts proceeds up to the isotopes around the mass number 64, specifically Zn and Se, when the accreted matter is metal poor with 5% of the solar abundance. Although the results may depend on the details of the burst modeling, which has been rapidly evolving recently, burst ashes with the mass number $\sim$ 50–60 are likely to be well exposed on the neutron star surface in some bursts.

Emergence of the edges in the cooling phase of the burst may be interpreted as

the change of the ionization degree of the burst ashes. Heavy elements in the burst photosphere are likely to be fully ionized when the temperature is high. When the photosphere cools down during the decay of the burst, heavy elements start to recombine, forming H-like and He-like ions. Similar tendency is reproduced in the model of neutron star atmospheres enriched with the burst ashes (Nättilä et al. 2015). When the luminosity is close to the Eddington limit, there exist very few structures, if any, in the calculated spectra, but then the prominent iron feature appears when the luminosity decreased to 10% of the Eddington limit. The burst observed here had a high luminosity close to the Eddington limit until 100 sec after the burst onset. We infer that burst ashes were almost fully ionized in this phase. After $\sim$ 100 sec, luminosities of the photosphere gradually decreased and H-like ions started to be formed in the atmosphere. This interpretation is also consistent with the time variations of the edge parameters in figure 3.12.

The gravitational redshifts can be evaluated from the edge energies, if the above interpretation is correct. The theoretical edge energies of H-like ions of Fe and Zn are 9.28 keV and 12.39 keV, respectively[1]. Thus, the observed edge energies must be gravitationally redshifted by $1 + z = 1.49 \pm 0.04$ on average, where two types of errors are included: one is statistical uncertainty, the other is systematic uncertainty associated with the assumed spin-frequency range, 0.6–1.2 kHz. In the same way, the edge energies of the other possible combination, Zn and Se, are 12.39 keV and 15.97 keV, respectively, which indicate the average gravitational redshift of $1 + z = 1.96 \pm 0.05$. These values may be a little too large; if we adopt a canonical value for the neutron star mass and radius, i.e. $1.4M_\odot$ and 10 km, the expected redshift becomes $1 + z = 1.31$. However, neutron stars in LMXB may have a larger mass due to the sustained mass accretion from the companion. In fact, two millisecond pulsars, possible descendant of LMXB, are found to have a mass of $2M_\odot$ (Demorest et al. 2010; Antoniadis et al. 2013). If we assume a plausible radius range of 11–15 km for a $2M_\odot$ neutron star, the gravitational redshift is estimated to be $1+z = 1.29$–1.48. This is compatible with the gravitational redshift obtained for the pair of Fe and Zn.

We then compare this result with the current theoretical mass-radius relations of the representative EOSs. Figure 4.6 shows the allowed region in the mass-radius diagram obtained from my result overlaid on the theoretical mass-radius curves compiled by Lattimer & Prakash (2001), some of which are already ruled out by the heavy neutron stars with a mass of 2 $M_\odot$. Figure 4.6 clearly shows that the allowed region for $1 + z = 1.96$ significantly exceed the line of the causality limit (see, e.g., Lattimer & Prakash 2007) and is therefore ruled out. On the other hand, the allowed region for $1 + z = 1.49$ shows no such conflict. It is consistent with those of all possible EOSs for normal matter such as neutron and proton. Based on this consideration, we consider that the gravitational redshift of $1 + z = 1.49$ is plausible. If we take this redshift, the radius of the neutron star becomes 8–11 km for the plausible mass range of 1.4–2 $M_\odot$. The neutron star may have has the heavier mass than an isolated neutron star with a typical mass of 1.4 $M_\odot$, because no possible EOSs exist in the allowed region below $\sim$ 1.8 $M_\odot$.

[1] http://xdb.lbl.gov/Section1/Sec_1-8.pdf

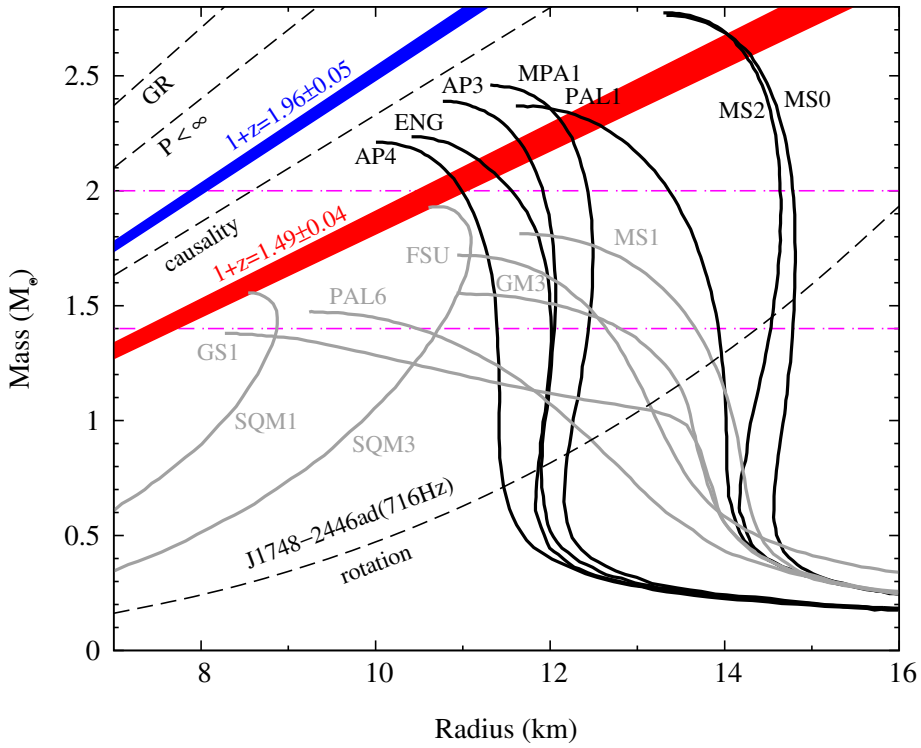

Figure 4.6: Various mass-radius curves of neutron stars for representative EOSs compiled by Lattimer & Prakash (2007). The dark-grey curves indicate the EOSs which is ruled out by the discovery of neutron stars with a mass of 2 $M_\odot$, and black curves not ruled out. The red- and blue-shaded regions show the observational constraint from the GRS 1747−312 surface gravitational redshifts of $1+z = 1.49 \pm 0.04$ and 1.96 ± 0.05, respectively. The widths of the regions represent errors in the 90% confidence limit. See text for details of the errors. The region between magenta dot-dashed lines indicates a plausible mass range of the neutron stars in LMXBs, 1.4–2.0 $M_\odot$.

4.4 Unique Nature of the Burst from GRS 1747−312

We consider here why absorption edges are formed on the neutron star surfaces have never been detected in other PRE bursts. The edges detected here are relatively deep with $\tau_{\rm edge} \sim 1.56$ and 2.85 and would have been easily detectable with the RXTE PCA, and possibly with detectors onboard BeppoSAX (Boella et al. 1997). Many PRE bursts have been detected with BeppoSAX and RXTE. For example, RXTE detection of 247 PRE bursts from 32 burst sources (as of July 2007) was reported by Galloway et al. (2008). Twenty four superexpansion bursts (extremes of PRE bursts) detected with BeppoSAX were reported in in't Zand & Weinberg (2010). Nevertheless, none of the reported bursts shows the deep edge-features detected here. Therefore, simple PRE may not be enough to form the absorption edges. In that sense, it may not be appropriate to interpret the edges in the context of non-Planckian spectrum, because the burst from GRS 1747−312 is not exceptional in luminosity and temperature.

A unique property of GRS 1747−312 is its faint X-ray emission. Luminosity of the persistent emission from GRS 1747−312 during the observation with Suzaku was $\sim 1.2 \times 10^{35}$ erg s^{-1}. On the other hand, most of burst sources reported in literature have the persistent luminosity higher than $\sim 10^{36}$ erg s^{-1} (Galloway et al. 2008). This selection may be an instrumental bias due to the sensitivity limit of the RXTE PCA. Because the burst rate decreases at lower luminosity, wide-field coverage may be necessary to catch bursts from dim sources. The Wide Field Cameras (Jager et al. 1997) onboard BeppoSAX observed 9 X-ray bursts without detectable persistent emission (Cornelisse et al. 2004). The typical upper limits of the persistent emission are $\sim 10^{36}$ erg s^{-1}. No spectral characteristics are reported for these bursts probably due to the poor statistics. As such, our knowledge on the bursts at the luminosity level of $\sim 10^{35}$ erg s^{-1} is still very limited.

One of the PRE bursts observed with RXTE from GRS 1747−312 may have occurred during the very low-luminosity state (in't Zand et al. 2003b). The upper limit of the persistent emission of $< 6 \times 10^{35}$ erg s^{-1} was inferred from the data of the scan observations that were performed regularly around the epoch of the burst occurrence. Thus, the burst may have occurred as the persistent luminosity level similar to the burst detected here. The burst showed a strong PRE with radius expansion by a factor of > 40, where the expansion was delayed from the onset by 20 sec. A broad-line feature was detected at 4.9 keV near the peak of PRE, but no spectral feature during the decay was reported. Although the nature of the broad-line feature is not known, burst ashes may be involved in producing 4.9-keV feature. If this is the case, bursts that occur during low-luminosity state may have a higher probability to produce atomic features, which can be observed in its energy spectrum, due to the burst ashes. Although it is difficult to draw a firm conclusion, the low persistent-luminosity is possibly related to the unique spectral feature of the burst from GRS 1747−312.

Chapter 5

Conclusion

We analyzed a thermonuclear X-ray burst from GRS 1747−312 observed with Suzaku to constrain the mass-radius relation of neutron stars. In particular, we focused on a study of the energy spectrum during the cooling phase of the burst. The time-resolved energy spectra of the burst were reproduced by the commonly applicable absorbed blackbody model most of time, but significant deviation was detected in the late cooling phase. The deviation was due to a clear roll off in the energy spectra above ~ 7 keV, which suddenly appeared in the cooling phase and became more prominent with time. In order to identify the origin of the spectral roll off, it was modeled by the combination of an absorbed blackbody and 1) a single absorption edge; 2) a single Doppler-smeared absorption edge; 3) two Doppler-smeared absorption edges; 4) a relativistically broadened emission line; 5) a reflection spectrum; 6) a non-Planckian correction for Comptonization of the black body and 7) partial-covering absorption. As a result, we found that the roll-off is most probably explained by two Doppler-smeared absorption edges of hydrogen-like Fe and Zn ions, which should be the major burst products involved to form the edges. According to this scenario, we can naturally interpret the emergence of the feature in the late cooling phase of the burst as the change of the ionization degree of the burst products. The burst products are expected to be ejected by the radiation-driven wind during the photospheric-radius expansion phase and be exposed on the neutron star surface later. If this interpretation is correct, the gravitational redshift is estimated to be 1.49 ± 0.04, corresponding to a neutron-star radius range of 8–11 km for an assumed neutron-star mass range of 1.4–2.0 solar mass. Because the absorption edge is not completely smeared out despite of the rapid spin of the neutron star, this can be a powerful observational tool to measure the gravitational redshift of neutron stars. This means that further detections of similar spectral feature from other burst sources are prospective in the near future, using the archive data of other X-ray astronomy satellites such as XMM-Newton and NuSTAR which is NASA's latest high-energy astrophysics observatory launched in 2012.

Appendix A

Doppler Smeared Absorption Edge (dpsmedge)

We assume that an absorption edge is formed at the neutron star surface that is spinning at a frequency of $\nu_{\rm ns}$. If the neutron star is observed by a distant observer, the edge is smeared due to the rotational broadening. We construct a model function to describe the smeared edge under the assumption of Newtonian limit, ignoring the relativistic effects.

We take the zenith angle θ and the azimuthal angle ϕ over the hemisphere of the neutron star, which is visible by a distant observer. Then, the spectral function, $m(E')$, of an absorption edge formed at a surface element may be formulated as follows, taking account of the Doppler effect:

$$m(E') = \begin{cases} \exp\left[-\tau_{\rm edge}\left(\dfrac{E'}{E_{\rm edge}}\right)^{-3}\right] & (E' \geq E_{\rm edge}) \\ 1 & (E' < E_{\rm edge}), \end{cases}$$

where E' is the photon energies and is defined as $E' = E(1 - \beta \sin i \sin\theta \cos\phi)$, $\beta = 2\pi R_{\rm ns}\nu_{\rm ns}/c$ is the scale of rotational broadening, $R_{\rm ns}$ is the radius of a neutron star, i is the inclination angle of the neutron star's spin axis, and c is the speed of light. Therefore, the spectral shape, $M(E)$, observed by a distant observer is given by:

$$M(E) = \int d\phi \int \sin\theta d\theta \; w(\theta,\phi) \times m(E,\theta,\phi).$$

Here we have included a weight function, $w(\theta,\phi)$, to reflect the obliqueness of the surface element to the line of sight of the observer. The free parameters in $M(E)$ are optical depth of the edge $\tau_{\rm edge}$, the edge energy $E_{\rm edge}$, and the spin frequency of the neutron star $\nu_{\rm ns}$. This smeared-edge model is incorporated into XSPEC as a table model, and is used to fit the burst spectra.

We plot $M(E)$ for 4 different spin frequencies in figure B, assuming the edge energy and optical depth to be 7 keV and 1, respectively. As is apparent in figure B, the absorption edge on the neutron star surface is not completely smeared out even with the maximum spin frequency of the neutron star, 620 Hz.

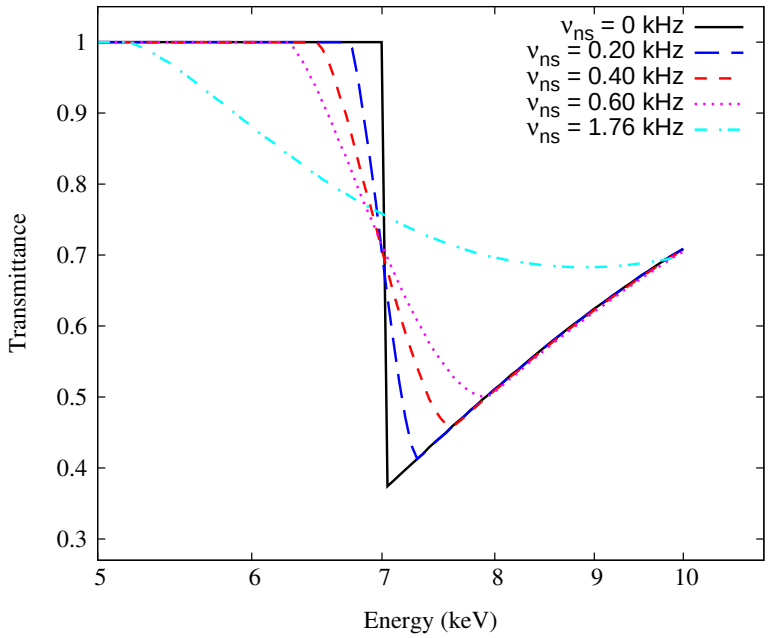

Figure A.1: Examples of dpsmedge model for 5 different spin frequencies: 0 kHz (solid line), 0.2 kHz (long-dashed line), 0.4 kHz (dashed line), 0.6 kHz (dotted line), and 1.76 kHz (dash-dotted line). The optical depth and the edge energy are assumed to be 1.0 and 7 keV, respectively.

Appendix B

Time-Resolved Energy Spectra of the Burst from GRS 1747−312

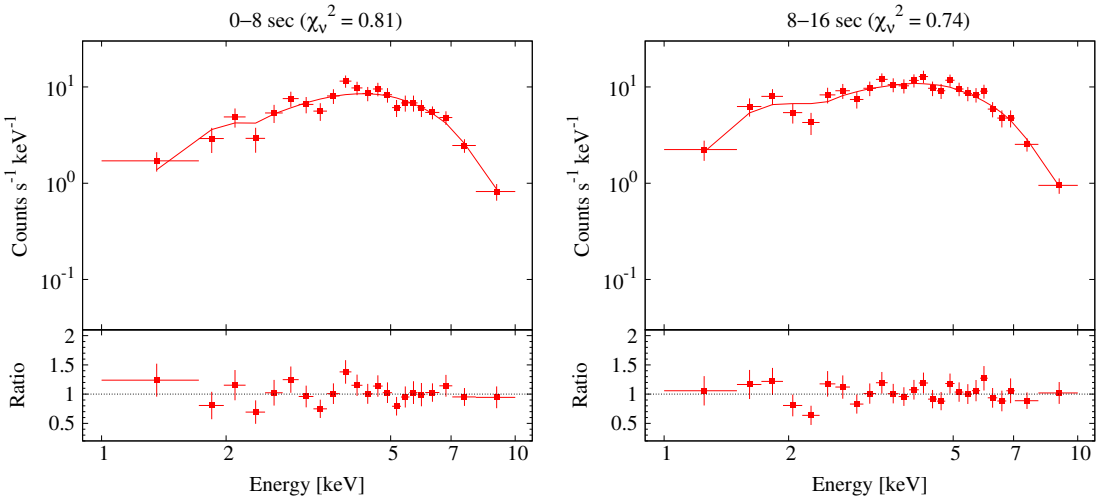

Figure B.1: Burst spectra from GRS 1747−312 every 8 sec in 1–10 keV are plotted in the upper panel. The filled squares are for the XIS 0 and 3 (FI-CCD) data. The solid lines indicate the best-fit models of an absorbed blackbody. The fit residuals are shown in the lower panel as ratio of the observed spectra to the best-fit models. The horizontal bars of the data points represent integration energy ranges, and the vertical bars errors in the 68% (1σ) confidence limit.

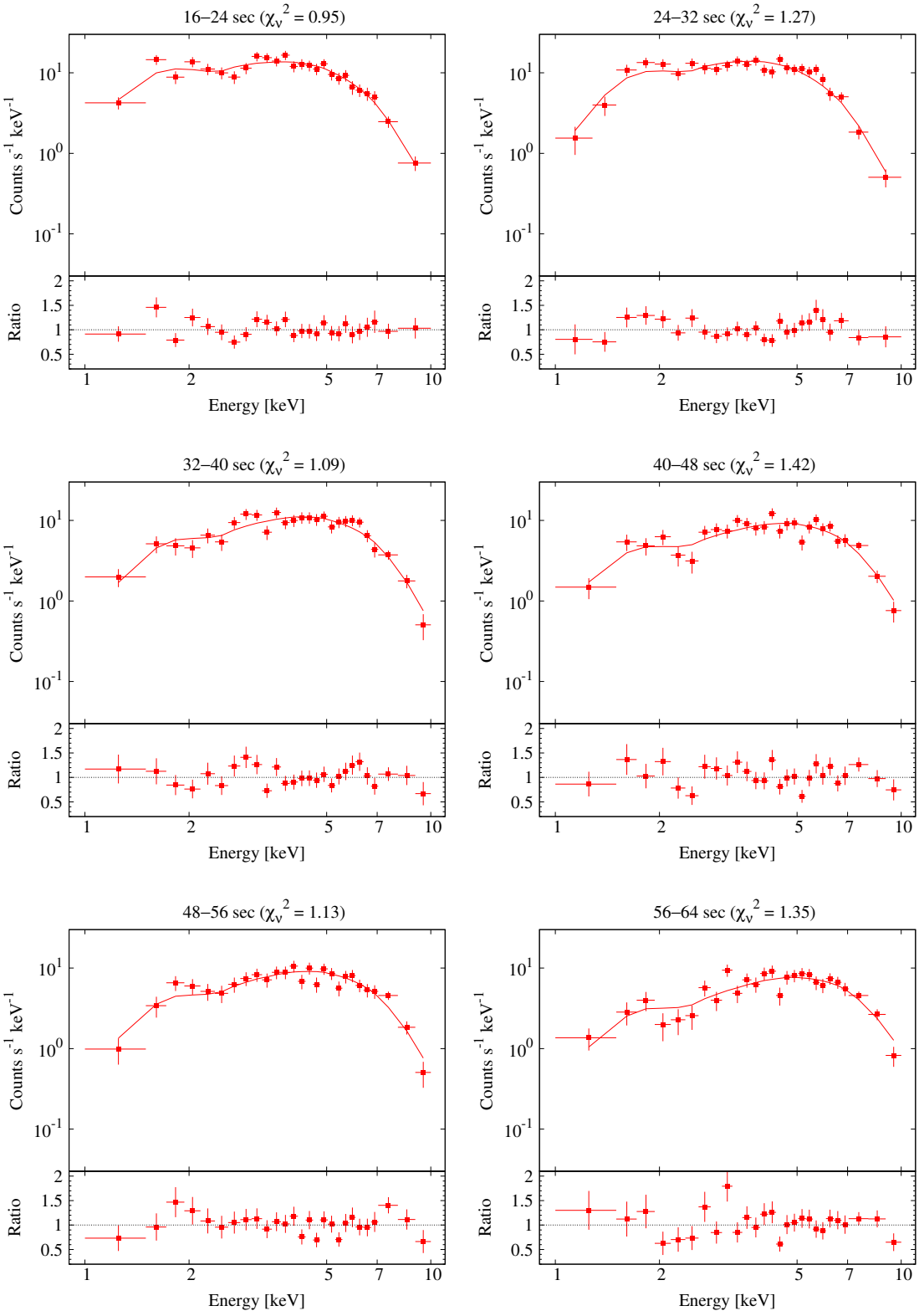

Figure B.2: Continued.

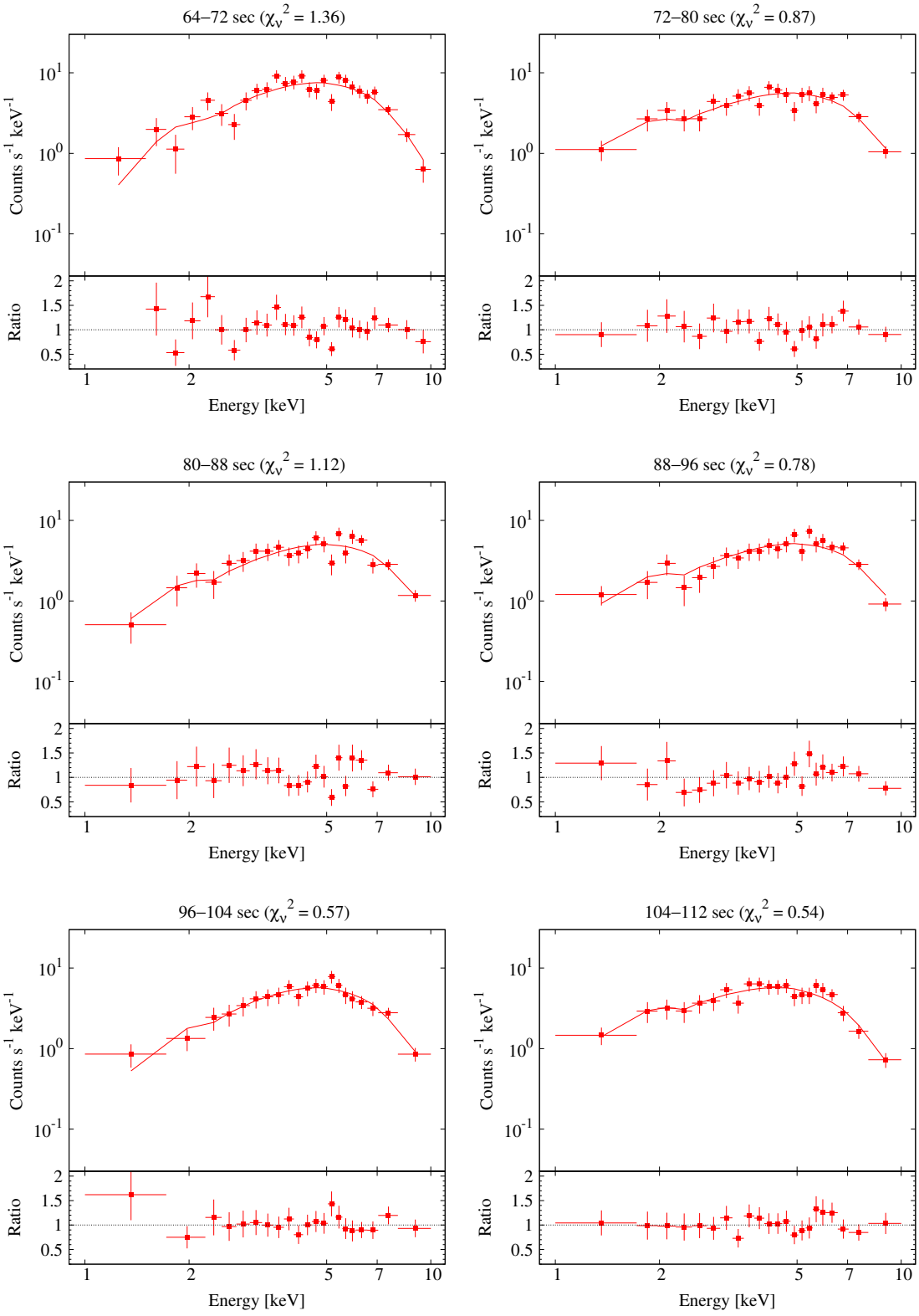

Figure B.3: Continued.

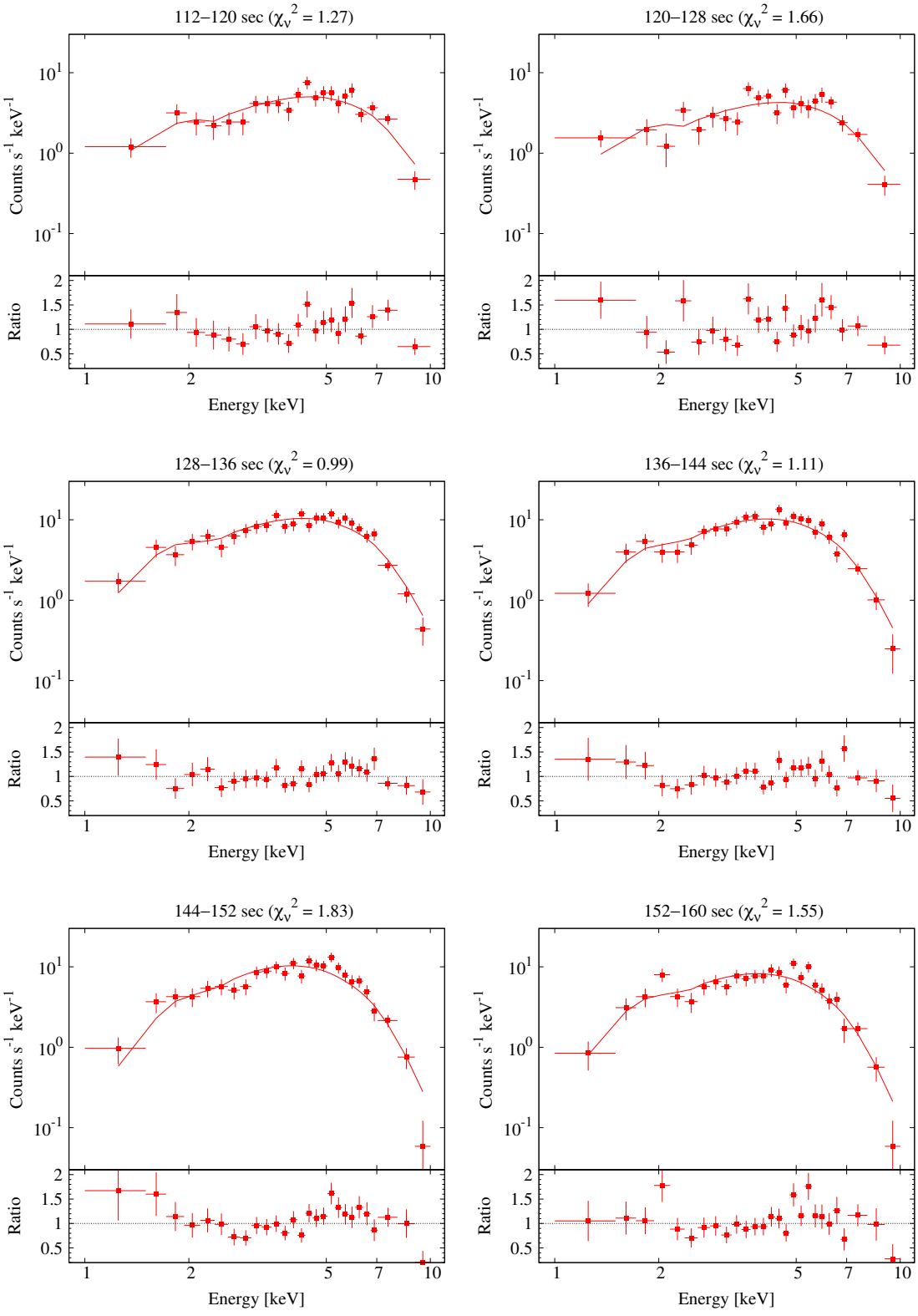

Figure B.4: Continued.

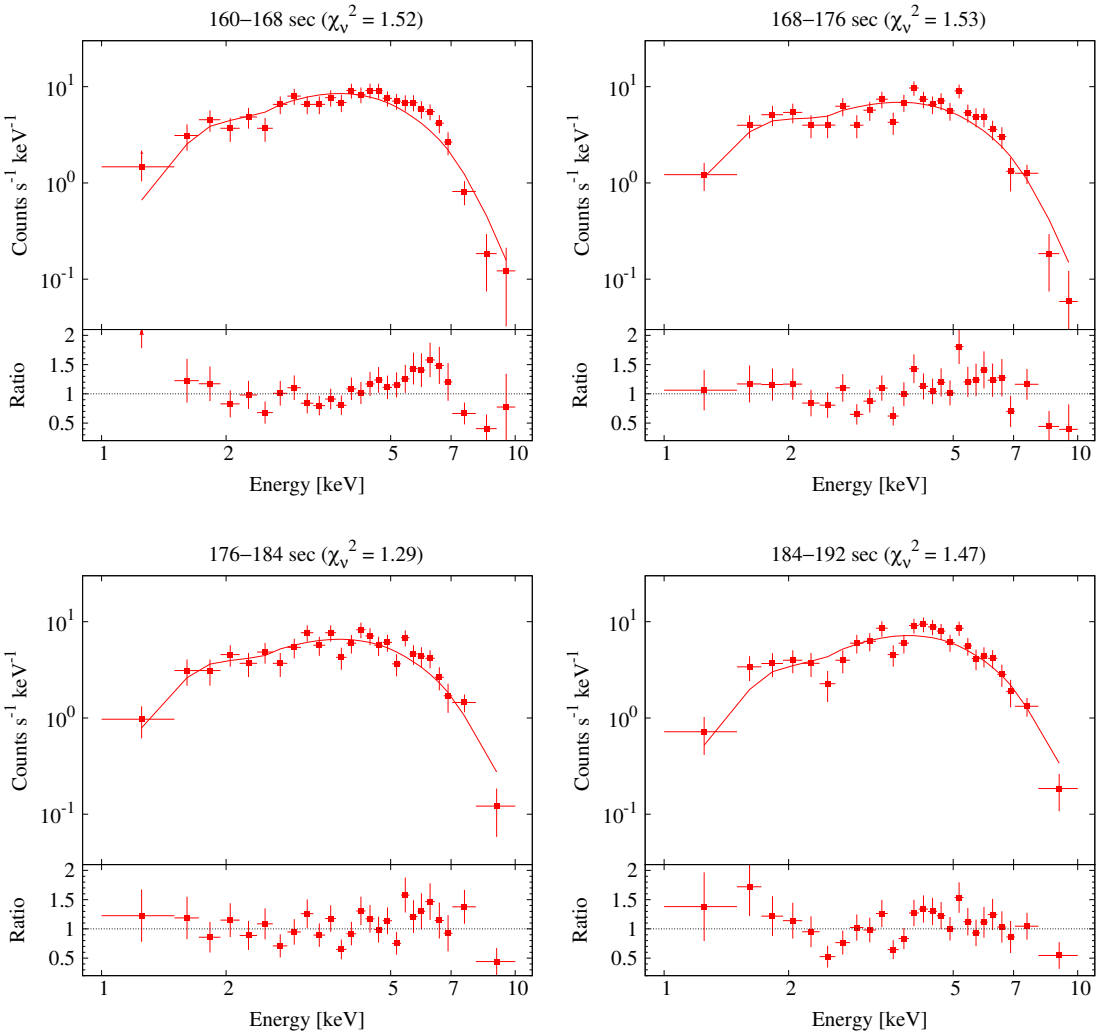

Figure B.5: Continued.

Bibliography

Akmal, A., & Pandharipande, V. R. 1997, Phys. Rev. C, 56, 2261

Antoniadis, J., et al. 2013, Science, 340, 448

Arnaud K. A. 1996, in ASP Conf. Ser., 101, Astronomical Data Analysis Software and Systems V, ed. G. H. Jacoby & J. Barnes (San Francisco: ASP), 17

Asai, K., & Dotani, T. 2006, PASJ, 58, 587

Barrière, N. M., et al. 2015, ApJ, 799, 123

Bhattacharya, D., & van den Heuvel, E. P. J. 1991, Phys. Rep., 203, 1

Bhattacharyya, S., Storohmayer, T. E., Miller, M. C., & Markwardt, C. B. 2005, ApJ, 619, 483

Bhattacharyya, S. 2010, Adv. Space Res., 45, 949

Bildsten, L. 1998, in The Many Faces of Neutron Stars, ed. R. Buccheri, J. van Paradijs, & A. Alpar (Dordrecht: Kluwer), 419

Bildsten, L. 2000, in AIP Conf. Ser. 522, Cosmic Explosions, ed. S. Holt & W. Zhang (Woodbury: AIP), 359

Bildsten, L., Chang, P., & Paerels, F. 2003, ApJ, 591, L29

Boella, G., Butler, R. C., Perola, G. C., Piro, L., Scarci, L., & Bleeker, J. 1997, A&AS, 122, 299

Bradt, H. V., Rothschild, R.E., & Swank, J.H. 1993, A&AS, 97, 355

Chang, P., Bildsen, L., & Wasserman, I. 2005, ApJ, 629, 998

Cornelisse, R., et al. 2004, Nucl. Phys. B Pro. Suppl., 132, 518

Cottam, J., Paerels, F., & Méndez, M. 2002, Nature, 420, 51

Cottam, J., Paerels, F., Méndez, M., Boirin, L., Lewin, W. H. G., Kuulkers, E., & Miller, J. M. 2008, ApJ, 672, 504

Cumming, A., & Macbeth, J. 2004, ApJ, 603, 37

Damen, E., Magnier, E., Lewin, W. H. G., Tan, J., Penninx, W., & van Paradijs, J. 1990, A&A, 237, 103

Demorest, P. B., Pennucci, T., Ransom, S. M., Roberts, M. S. E., & Hessels, J. W. T. 2010, Nature, 467, 1081

den Herder, J. W., et al. 2001, A&A, 365, L7

Done, C., Mulchaey, J. S., Mushotzky, R. F., & Arnaud, K. A. 1992, ApJ, 395, 275

Ebisuzaki, T. 1987, PASJ, 39, 287E

Engvik, L., Hjorth-Jensen, M., Osnes, E., Bao, G., & Østgaard, E. 1994, Phys. Rev. Lett., 73, 2650

Enoto, T., Nakazawa, K., Makishima, K., Rea, N., Hurley, K., & Shibata, S. 2010, ApJ, 722, 162

Fabian, A. C., Rees, M. J., Stella, L. & White, N. E. 1989, MNRAS, 238, 729

Fujimoto, M. Y., Hanawa, T., & Miyaji, S. 1981, ApJ, 247, 267

Fujimoto, M. Y., Sztajno, M., Lewin, W. H. G., & van Paradijs, J. 1987, ApJ, 319, 902

Galloway, D., Muno, M. P., Hartman, J. M., Psaltis, D., & Chakrabarty, D. 2008, ApJ, 179, 360

Gendreau, K. C., Arzoumanian, Z., & Okajima, T. 2012, in SPIE Conf. Ser., doi:10.1117/12.926396

Glendenning, N. K., & Moszkowski, S. A. 1991, Phys. Rev. Lett., 67, 2414

Glendenning, N. K., & Schaffner-Bielich, J. 1999, Phys. Rev. C., 60, 025803

Harding, A. K. 2013, Front. Phys., 8(6), 67

Harrison, F. A., et al. 2013, ApJ, 770, 103

Inoue, H. 2015, PASJ, submitted

in't Zand, J. J. M., et al. 2000, A&A, 355, 145

in't Zand, J. J. M., et al. 2003a, A&A, 406, 233

in't Zand, J. J. M., Strohmayer, T. E., Markwardt, C. B., & Swank, J. 2003b, A&A, 409, 659

in't Zand, J. J. M., & Weinberg, N. N. 2010, A&A, 520, A81

Jager, R., et al. 1997, A&AS, 125, 557

Jahoda, K., Markwardt, C. B., Radeva, Y., Rots, A. H., Stark, M. J., Swank, J. H., Strohmayer, T. E., & Zhang, W. 2006, ApJS, 163, 401

Jansen, F., et al. 2001, A&A, 365, L1

José, J., Moreno. F., Parikh, A., & Iliadis, A. 2010, ApJS, 189, 204

Kaaret, P., et al. 2006, ApJ, 657, 97

Kokubun, M., et al. 2007, PASJ, 59, S53

Koyama, K., et al. 2007, PASJ, 59, S23

Kuulkers, E., den Hartog, P. R., in't Zand, J. J. M., Verbunt, F. W. M., Harris, W. E., & Cocchi, M. 2003, A&A, 399, 663

Lattimer, J. M., & Prakash, M. 2001, ApJ, 550, 426

Lattimer, J. M., & Prakash, M. 2007, Phy. Rep., 442, 109

Lewin, W. H. G., van Paradijs, J., & Taam, R. E. 1993, Space Sci. Rev., 62, 223

Lewin, W. H. G., van Paradijs, J., & Taam, R. E. 1995, in X-Ray Binaries, ed. W. H. G. Lewin, J. van Paradijs, & E. P. J. van den Heuvel (Cambridge: Cambridge Univ. Press), 175

Liu, Q. E., van Paradijs, J., & van der Heuvel, E. P. J. 2006, A&A, 455, 1165

Liu, Q. E., van Paradijs, J., & van der Heuvel, E. P. J. 2007, A&A, 469, 807

Loeb, A. 2003, Phys. Rev. Lett., 91, 071103

Madej, J., Joss, P. C., & Rozanska, A. 2004, ApJ, 602, 904

Magdziarz, P., & Zdziarski, A. 1995, MNRAS, 273, 837

Magnier, E., Lewin, W. H. G., van Paradijs, J., Tan, J., Penninx, W., & Damen, E. 1989, MNRAS, 237, 729

Majczyna, A., Madej, J., Joss, P. C., & Różańska, A. 2005, A&A, 430, 643

Mitsuda, K., et al. 2007, PASJ, 59, S1

Müller, H., & Serot, B. D. 1996, Nucl. Phys. A, 606, 508

M̈ther, H., Prakash,M., & Ainsworth, T. L. 1987, Phys. Lett., B199, 469

Nakamura, N., Inoue, H., & Tanaka, Y. 1988, PASJ, 40, 209

Nath, N. R., Strohmayer, t. E., & Swank, J. H. 2002, ApJ, 564, 353

N*ättilä*, J., Suleimanov, V., Kajava, J., & Poutanen, J. A&A, 581 (2015) A83

Özel, F., & Psaltis, D. 2003, ApJ, 582, L31

Özel, F. 2013, Rep. Prog. Phys., 76, 016901

Parikh, A., José, J., Sala, G., & Iliadis, C. 2013, Prog. Part. Nucl. Phys., 69, 225

Pavlinsky, M. N., Grebenev, S. A., & Sunyaev, R. A. 1994, ApJ, 425, 110

Prakash, M., Ainsworth, T. L., & Lattimer, J. M. 1988, Phys. Rev. Lett., 61, 2518

Prakash, M., Cooke, J. R., & Lattimer, J. M. 1995, Phys. Rev., D52, 661

Predehl, P., Hasinger, G., & Verbunt, F. 1991, A&A, 246, L21

Saji, S., et al. 2015, PASJ, submitted

Serlemitsos, P. J., et al. 2007, PASJ, 59, S9

Shen, G., Horowitz, C. J., & O'Connor, E. 2011, Phys. Rev. C, 83, 065808

Strohmayer, T. E. 2001, Adv. Space Res., 28, 511

Strohmayer, T. E., & Brown, E. F. 2002, ApJ, 566, 1045

Suleimanov, V., Poutanen, J., & Werner, K. 2011, A&A, 527, A139

Suleimanov, V., Poutanen, J., & Werner, K. 2012, A&A, 545, A120

Takahashi, T., et al. 2007, PASJ, 59, S35

Tanaka et al. 1984, PASJ, 36, 641

Taylor, B.G., Andresen, R.D., Peacock, A., & Zobl, R. 1981, Space Sci. Rev., 30, 479.

Uchiyama, Y., et al. 2008, PASJ, 60, S35

van Paradijs, J., Dotani, T., Tanaka, Y., & Tsuru, T. 1989, PASJ, 42, 633

Waki, I., Inoue, H., Koyama, K., Matsuoka, M., Murakami, T., Ogawara, Y., Ohashi, T., & Tanaka, Y. 1984, PASJ, 36, 819

Wallace, R. K., & Woosley, S. E. 1981, ApJS, 45, 389

Weinberg, N. N., Bildsten, L., & Schatz, H. 2005, ApJ, 639, 1018

Woosley, S. E., et al. 2004, ApJS, 151, 75

Yamada, S., et al. 2012, PASJ, 64, 53

Acknowledgments

I have been supported by many people during the three years of my PhD life and this thesis would not have been materialized without their help.

First, I would like to show my greatest appreciation to my supervisor Professor Tadayasu Dotani. His enormous support and insightful comments were invaluable during the course of this study.

I would also like to express my gratitude to assistant professor Yoshitomo Maeda in ISAS/JAXA and Dr. Hideyuki Mori in NASA/GSFC for giving the beginning of this study.

I appreciate to other members in Dotani laboratory (CCD group) and my colleagues at ISAS/JAXA: associate professor Masanobu Ozaki, Mr. Chikara Natsukari, Mr. Hiroshi Tomida, Dr. Satoru Katsuda, Dr. Shutaro Ueda, Mr. Keisuke Kondo, Mr. Shinji Kai, Mr. Shunsuke Imai, Mrs. Aya Koyama, Mrs. Asuka Tsuji, Mr. Yuto Ichinohe, Mr. Kenichiro Nagayoshi, and Mr. Ryo Yamamoto. I was able to have a good time in ISAS/JAXA thanks to their support and warm encouragement.

Finally, special thanks to my parents, sisters, and family: Mr. Kiyochika Iwai, Mrs. Junko Iwai, Mrs. Shima Inada, Ms. Shiho Iwai, Mrs. Yumi Iwai and Mr. Haruchika Iwai.

This work was supported by Grant-in-Aid for JSPS Fellows Grant Number 15J11851 and JSPS KAKENHI Grant Number 24105007.

It was a wonderful PhD life! I am grateful to all of people supporting my PhD life. Thank you so much.

Masachika Iwai